



A theoretical model to analyze the Central to Eastern Pacific El Niño continuum

Yves Morel, Sulian Thual, Thierry Delcroix, Nick Hall, Gaël Alory

► To cite this version:

Yves Morel, Sulian Thual, Thierry Delcroix, Nick Hall, Gaël Alory. A theoretical model to analyze the Central to Eastern Pacific El Niño continuum. *Ocean Modelling*, 2018, 130, pp.140-159. 10.1016/j.ocemod.2018.07.006 . hal-02349698

HAL Id: hal-02349698

<https://hal.science/hal-02349698>

Submitted on 5 Nov 2019

HAL is a multi-disciplinary open access archive for the deposit and dissemination of scientific research documents, whether they are published or not. The documents may come from teaching and research institutions in France or abroad, or from public or private research centers.

L'archive ouverte pluridisciplinaire **HAL**, est destinée au dépôt et à la diffusion de documents scientifiques de niveau recherche, publiés ou non, émanant des établissements d'enseignement et de recherche français ou étrangers, des laboratoires publics ou privés.

1 A theoretical model to analyze the Central to Eastern
2 Pacific El Niño continuum

3 Yves Morel^{1,*}, Sulian Thual^{2,*}, Thierry Delcroix^{1,*}, Nick Hall^{1,*}, Gaël
4 Alory^{1,*}

5 **Abstract**

6 A current scientific issue of great interest is to understand the mecha-
7 nisms leading to the localization of El Niño events either in the Central (CP)
8 or Eastern Pacific (EP). For this, we derive a reduced gravity mixed layer
9 model for the equatorial ocean with simple nonlinearities, diabatic effects
10 and zonally varying background characteristics. Using the model, we study
11 the propagation of an equatorial Kelvin wave from an initial perturbation.
12 An approximate analytical solution is found for the evolution of the max-
13 imum density (or temperature) anomaly created during the passage of the
14 wave. Density anomalies can either peak in the CP or continuously increase
15 until reaching the EP, which is representative of both types of El Niño. Sen-
16 sitivity tests reveal that both the zonally varying background stratification
17 and diabatic effects are important to determine the density pattern. The EP
18 pattern is obtained for smooth background variations while the CP pattern
19 requires a frontal background structure. Using numerical experiments, we
20 then show how consecutive Kelvin waves can lead to the transition from a
21 CP to an EP pattern. The present theoretical results provide useful insights
22 for understanding El Niño dynamics and diversity in more complete models
23 and observations.

24 *Keywords:* Equatorial Kelvin waves, mixed layer, El Niño.

*Corresponding authors
Preprint submitted to Ocean Modelling
Email addresses: Yves.Morel@legos.obs-mip.fr (Yves Morel), November 5, 2019
Sulian.Thual@gmail.com (Sulian Thual), Thierry.Delcroix@legos.obs-mip.fr
(Thierry Delcroix), Nick.Hall@legos.obs-mip.fr (Nick Hall),
gael.alory@legos.obs-mip.fr (Gaël Alory)

¹LEGOS, University of Toulouse, CNES, CNRS, IRD, UPS, Toulouse, France

²Center for Atmosphere and Ocean Science, Courant Institute of Mathematical Sci-
ences, New York University, New York, USA

25 1. Introduction

26 1.1. *El Niño*

27 The El Niño-Southern Oscillation (ENSO) is one of the most studied
28 phenomena in oceanic and atmospheric sciences, owing to its major conse-
29 quences on the tropical Pacific climate as well as its impact through world-
30 wide teleconnections. The ENSO consists of alternating periods of anoma-
31 lously warm El Niño conditions and cold La Niña conditions every 2 to
32 7 years, with considerable irregularity in strength, duration and structure
33 of these events (Neelin et al., 1998; Dijkstra, 2006; Clarke, 2008). One of
34 the striking consequence of this phenomenon is the occurrence and westward
35 propagation of a sea surface temperature (SST) anomaly, which has major
36 consequences for the tropical Pacific climate and fisheries. Many studies
37 have been carried out but the details of the mechanisms setting up an El
38 Niño event and driving its diversity and possible evolution still need to be
39 better understood to be successfully modeled and predicted (Wang and Pi-
40 caut, 2004; Ashok and Yamagata, 2009; Guilyardi et al., 2009; Cai et al.,
41 2015; Capotondi et al., 2015).

42 1.2. *EP vs CP*

43 The mechanisms and prediction of El Niño events remain elusive despite
44 their important impacts because each of them shows unique and distinctive
45 features. In fact, El Niño events vary greatly in strength, evolution and
46 localization in the recent observational record. A current scientific issue of
47 great interest is to understand the mechanisms leading to the localization
48 of El Niño sea surface temperature (SST) anomalies either in the Central

49 (CP) or Eastern Pacific (EP). Observations indicate two different fates for
 50 El Niño events: the SST anomaly propagates up to the eastern Pacific (EP)
 51 or stalls in the central Pacific (CP). While extreme El Niño events such
 52 as those of 1982/83, 1997/98 have maximal SST anomalies in the eastern
 53 Pacific, there have been many examples of moderates CP events in the
 54 recent record (Ashok et al., 2007; Kug et al., 2009; Capotondi et al., 2015).
 55 The recent extreme El Niño event of 2015/2016 showed SST anomalies in
 56 both the central and eastern Pacific (Paek et al., 2016; Chen et al., 2017a).
 57 Observational studies also show that there has been a constant increase in
 58 the occurrence of CP El Niño events during the last centuries and decades
 59 (Liu et al., 2017), and modeling studies suggest that such a trend would
 60 continue in an anthropogenic warming climate scenario (Yeh et al., 2009;
 61 Cai et al., 2014).

62 *1.3. modeling of EP vs CP*

63 ENSO diversity presents a major challenge to Coupled General Circula-
 64 tion Models (CGCMs, see Clarke et al., 2007). In fact, most of those CGCMs
 65 still show deficiencies in simulating the diversity of El Niño amplitude, lo-
 66 calization and frequency due to systematic biases in the mean climate and
 67 seasonal cycle of the tropical Pacific (Bellenger et al., 2014). However, there
 68 have been examples of GCM improvements for simulating both the CP and
 69 EP El Niños (Kug et al., 2010; Dewitte et al., 2012). CP and EP El Niños are
 70 also captured in several simpler models based on different recipes. The ear-
 71 liest models of both conceptual and intermediate complexity usually focused
 72 on the dynamics of EP El Niño events only (Zebiak and Cane, 1987; Suarez
 73 and Schopf, 1988; Jin, 1997). More recent theoretical studies suggest that
 74 the dynamics of the CP and EP events involve different processes. While

75 studies usually agree that the EP El Niño is driven by thermocline feedback
76 in the eastern Pacific (An and Jin, 2001; Dewitte et al., 2013), several mech-
77 anisms have been proposed for the dynamics of the CP El Niño. Simple
78 models depict the CP El Niño as resulting, for example, from the zonal ad-
79 vection of the warm pool SST edge (Picaut et al., 1997; Clarke et al., 2007)
80 or the nonlinear advection of SST anomalies in the central Pacific (Chen
81 et al., 2017b). Fedorov et al. (2015) and Chen et al. (2015) suggest that the
82 different EP and CP flavors may result from different responses to state-
83 dependent westerly wind bursts. In contrast, Ren and Jin (2013) suggest
84 that the CP and EP El Niños can be represented as two independent modes
85 of the simple recharge-discharge model from (Jin, 1997).

86 *1.4. EP / CP continuum*

87 The above bimodal separation of EP and CP events has been questioned
88 and recent consensus is that they are part of a continuum. For instance,
89 Capotondi et al. (2015) analyse the diversity of El Niño events in nature,
90 pointing to the CP/EP continuum that is evidenced by the overlapping
91 localization of SSTs from the central to eastern Pacific. Takahashi et al.
92 (2011) analyses empirical orthogonal functions of SSTs suggesting that the
93 CP and EP El Niño regimes are non-separable and interact nonlinearly.

94 *1.5. Coupled instability studies*

95 Insight on ENSO dynamics has also been gained by analyzing the prop-
96 agation of coupled (ocean and atmosphere) equatorial waves using linear
97 instability methods. These studies focus on the coupling between the ocean
98 mixed layer(s) and atmosphere to explain the growth of the SST anomaly
99 (Hirst, 1986; Pontaud and Thual, 1998; Thual et al., 2012). While the

100 above studies consider homogeneous background conditions (i.e. constant
 101 with space) for simplicity, several studies have also analyzed the effect of
 102 varying background characteristics on coupled instabilities. For this, nu-
 103 merical experiments are usually considered to solve the nonlinear dynamics
 104 while simplified analytical results may be obtained in some instances using
 105 common approximations such as the method of multiple scales (e.g. WKB
 106 approximation, Busalacchi and Cane, 1988; Yang and Yu, 1992). One of
 107 the most important background characteristics that affects equatorial wave
 108 propagation appears to be zonal changes in ocean stratification (e.g. in
 109 thermocline depth), which are quite marked in the equatorial Pacific. For
 110 example, a shoaling thermocline can significantly modify the characteristics
 111 of an equatorial Kelvin wave including its amplitude, deformation radius
 112 and baroclinic structure in addition to reflecting a significant portion of
 113 the flux westward (Long and Chang., 1990; Fedorov and Melville, 2000).
 114 Observational studies further suggest that this type of nonlinear equatorial
 115 wave dynamics is at work to some extent in nature (e.g. Zheng et al., 1998;
 116 Cravatte et al., 2003; Bosc and Delcroix, 2008). Such an analysis can be
 117 extended to study coupled ocean-atmosphere basin modes in the presence
 118 of boundary reflections at the eastern and western edges of the equatorial
 119 Pacific (Wakata and Sarachik, 1991; Yang and O'Brien, 1993; Wu and An-
 120 derson, 1995). While the above studies detail the propagation mechanisms
 121 of equatorial waves, they do not necessarily relate them to the mechanisms
 122 of the EP and CP continuum of El Niño events.

123 *1.6. Article scope and structure*

124 An important point is thus that very few simple process-oriented studies
 125 address the theoretical aspects of the CP El Niño or the continuity between

CP and EP El Niño events (Capotondi et al., 2015). This is what we propose in the present study. Our aim is not to reproduce the complete evolution of El Niño events. We restrict our attention to the propagation of an equatorial Kelvin wave, once it has been formed, and analyze its effect on the modification of the mixed layer temperature, here associated with density.

To do so, we derive a reduced gravity mixed layer model for the equatorial ocean with simple nonlinearities, diabatic effects and zonally varying background characteristics (section 2). We derive an analytical expression for zonal shape of the wave and the density anomaly it generates under adiabatic (section 3) or diabatic (section 4) evolution. We analyze under which circumstances density anomalies can either peak in the CP or continuously increase until reaching the EP. The sensitivity to several parameters is also studied (section 5). Finally, using numerical experiments, we show how consecutive Kelvin waves can lead to the transition from a CP to an EP pattern (section 6).

2. The model

2.1. Simplified equations : a bulk mixed layer 1D model

We here focus on the evolution of an equatorial Kelvin wave in a variable background state. We simplify the equations as much as possible to only retain some aspects of the dynamics: pressure gradient, horizontal advection, divergence of the horizontal velocity field and the stretching effect associated with the vertical motion of the base of the thermocline ($w(z = -H) = \frac{dH}{dt}$). These are the main processes responsible for the wave propagation and for the impact of the wave on tracers such as density. The most simple model, able to reproduce the main features of equatorial Kelvin waves, is a bulk

151 mixed layer reduced gravity model along the equator. The model is thus 1D
 152 in the longitude direction, the meridional velocity $V = 0$ and the Coriolis
 153 term are neglected (see Fig. 1). The momentum conservation, continuity
 154 and buoyancy evolution equations then read (see Gill, 1982; Anderson and
 155 McCreary, 1985; Benestad, 1997; Neelin et al., 1998; Dijkstra and Burgers,
 156 2002, and Appendix A for further details and justification of the model):

$$\begin{aligned}
 \partial_t U + U \cdot \partial_x U &= -\frac{\partial_x P}{\rho_{ref}} + F^U, \\
 \partial_t H + \partial_x (H U) &= F^H, \\
 \partial_t (\rho_s H) + \partial_x (\rho_s H U) &= F^\Theta,
 \end{aligned} \tag{1}$$

157 where U is the longitudinal velocity field, P is the hydrostatic pressure,
 158 ρ_{ref} is a constant reference density such that the total density in the mixed
 159 layer is $\rho_s^{tot} = \rho_{ref} + \rho_s$, where ρ_s is the zonal variation of the mixed layer
 160 density, and H is the mixed layer thickness. F^U , F^H and F^Θ are forcing
 161 terms representing all effects necessary to explain the evolution of averaged
 162 physical quantities in the mixed layer, including all forcing effects (wind
 163 stress, vertical mixing, buoyancy/heat flux, effect of instabilities).

164 The dynamics is intensified in the upper layer and the layers below are
 165 considered at rest, so that the pressure anomaly P can be expressed as a
 166 function of the mixed layer thickness and density:

$$P \simeq g (\rho_b - \rho_s^{tot}) H, \tag{2}$$

167 where $g = 9.81 \text{ m.s}^{-2}$ is the earth gravity and ρ_b the density of the lower
 168 layer (at rest). If we further consider that the lower layer density variation

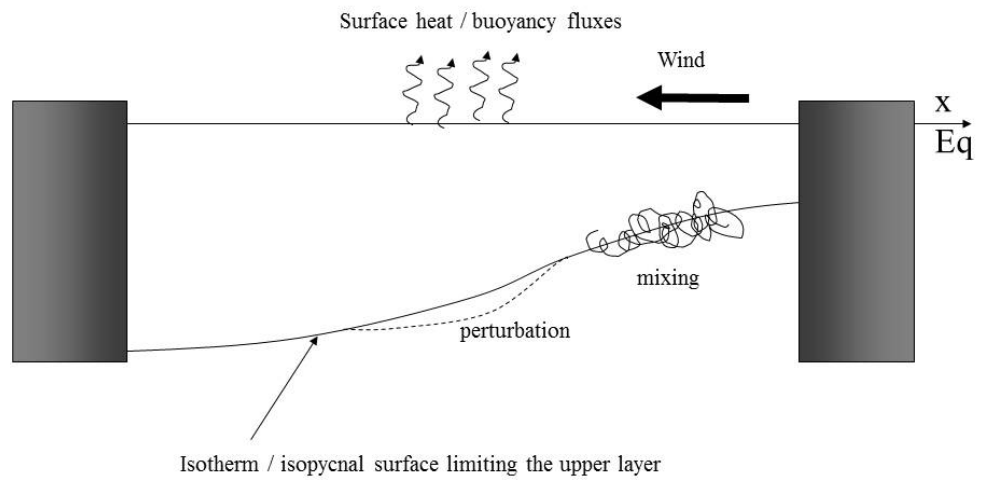


Figure 1: 1D (along Equator) configuration considered in the study.

169 ρ_b is negligible, we can set $\rho_{ref} = \rho_b$ and Eq. 1 become:

$$\begin{aligned}
\partial_t U + U \partial_x U &= \partial_x(\Theta) + F^U, \\
\partial_t H + \partial_x(H U) &= F^H, \\
\partial_t \Theta + \partial_x(\Theta U) &= F^\Theta,
\end{aligned} \tag{3}$$

170 where $\Theta = g\rho_s H/\rho_{ref}$ measures the local buoyancy (\approx heat) content of the
171 upper layer. Note that, as ρ_b is taken as the reference density ρ_s and Θ are
172 negative. Tables D.2 and D.3 in Appendix D summarize all variables and
173 parameters used in the present study.

174 As mentioned above, Eq. 3 are very simplified but retain the basic
175 dynamics of Kelvin wave evolution. Other processes that have been proven
176 to be important for ENSO (ocean/atmosphere fluxes, mixing at the base of
177 the mixed layer, effects of vertical variations within the upper layer, ..., see
178 Chen et al., 2016, for instance) will be parameterized through the forcing
179 terms F (see below).

180 2.2. Configuration

181 We hypothesize that there exists a known mean steady (e.g. slowly vary-
182 ing with respect to the wave propagation) state, U_o , H_o , $\Theta_o = g\rho_o H_o/\rho_{ref}$,
183 maintained by forcings F_o^U , F_o^H and F_o^Θ . The forcing terms can be calcu-
184 lated from the mean state using Eq. 3:

$$\begin{aligned}
F_o^U &= U_o \partial_x U_o - \partial_x(\Theta_o), \\
F_o^H &= \partial_x(H_o U_o), \\
F_o^\Theta &= \partial_x(\Theta_o U_o).
\end{aligned} \tag{4}$$

185 Note that the basic state forcing terms F_o should comprise all processes
186 maintaining the mean state: mean forcing terms and the mean contribution

187 of mixing or fluxes due to quadratic transient interactions. The Kelvin
 188 wave solutions we obtain below are perturbations of our imposed basic state
 189 and we consider them separately from any background transient activity
 190 maintaining the basic state.

191 We analyze the evolution of perturbations u , h , θ around the mean state
 192 and, with the decomposition $U = U_o + u$, $H = H_o + h$, $\Theta = \Theta_o + \theta$, the
 193 linearized equations for the perturbations are:

$$\begin{aligned}\partial_t u + \partial_x(U_o u) &= \partial_x(\theta) + \delta F^U, \\ \partial_t h + \partial_x(H_o u + h U_o) &= \delta F^H, \\ \partial_t \theta + \partial_x(\Theta_o u + \theta U_o) &= \delta F^\Theta,\end{aligned}\tag{5}$$

194 with $\delta F^X = F^X - F_o^X$. Hereafter, δF^X , if not neglected, will be parame-
 195 terized as a Newtonian cooling (see below). We will propose approximate
 196 analytical solutions of Eq. 5 and we will compare them to numerical solu-
 197 tions of the full nonlinear equations 3.

198 2.3. Density equation

199 The surface density perturbation evolution equation can be re-derived
 200 from Eq. 3 and using $\rho_s = \rho_{ref}\Theta/gH$:

$$\partial_t \rho_s + U \partial_x(\rho_s) = \frac{\rho_{ref}}{gH} F^\Theta - \frac{\rho_s}{H} F^H.\tag{6}$$

201 For gravity waves, U , H and Θ exhibit a propagating signal at first order,
 202 but density does not exhibit the same evolution: it is a tracer and it evolves
 203 under the influence of advection and diabatic forcing. As a result, for the
 204 numerical model with the full nonlinear Eq. 3, density can be diagnosed from
 205 the numerical Θ and H . This is not the case for the analytical calculations,
 206 which yield approximate, linear -propagating- solutions for U , H , Θ . The

analytical calculation of density requires us to solve Eq. 6 forced by the linear solution of Eq. 5 (see below and Appendix C). We also set $\rho_s = \rho_o + \rho$ where ρ is the density perturbation generated by the wave (see tables D.2 in Appendix D for a definition of all variables).

3. Results for linear waves in adiabatic conditions

3.1. Analytical solutions in adiabatic conditions

We present here analytical solutions for the linearized Eq. 5 in the case of homogenous or zonally varying background equilibrium state under adiabatic conditions (i.e. no forcing terms, $\delta F^X = 0$).

First, if the background equilibrium state is homogeneous (U_o , Θ_o , H_o do not vary) and we neglect forcing terms, Eq. 5 reverts to the well known gravity wave model, whose solution is:

$$\begin{aligned} u &= -g\rho_o/(\rho_{ref}C_o) [h^+(x - (U_o + C_o)t) - h^-(x - (U_o - C_o)t)], \\ h &= [h^+(x - (U_o + C_o)t) + h^-(x - (U_o - C_o)t)], \\ \theta &= g\rho_o/\rho_{ref} [h^+(x - (U_o + C_o)t) + h^-(x - (U_o - C_o)t)], \end{aligned} \quad (7)$$

Here $C_o = \sqrt{-\Theta_o}$ is the gravity wave propagation speed, h^+ and h^- are two functions defined from the initial conditions and corresponding to the eastward and westward propagation of the initial perturbation. As stated above, in the following we will consider eastward propagating waves. Note the buoyancy anomaly θ is proportional to the volume anomaly h and the wave is non-dispersive. The density anomaly is null. These are well known results for gravity waves.

Secondly, when the background state varies, the previous results are no longer valid and the equations are much more complicated. Giese and Harrison (1990) have addressed this problem and have proposed expressions

for the evolution of the wave amplitude when different mixed layer characteristics exist between the western and eastern equatorial Pacific. In their calculations, they neglected the background velocity field U_o , which is an approximation we will use too. We have here adapted and extended their results and calculated approximate solutions (see Appendix B) for our specific configuration. We get:

$$\begin{aligned}\theta &= \frac{C_o(x=x_o)^{1/2}}{C_o(x)^{1/2}} \theta_o(x/C(x) - t), \\ u &= \frac{\theta}{C_o(x)} = \frac{C_o(x=x_o)^{1/2}}{C_o(x)^{3/2}} \theta_o(x/C(x) - t), \\ h &= \frac{\rho_{ref}\theta}{g\rho_o(x)} = \frac{\rho_{ref}C_o(x=x_o)^{1/2}}{g\rho_o(x)C_o(x)^{1/2}} \theta_o(x/C(x) - t),\end{aligned}\quad (8)$$

where

$$\frac{x}{C(x)} = \int_{x_o}^x \frac{dx}{C_o(x)}, \quad (9)$$

Here again $C_o = \sqrt{-\Theta_o}$ is the gravity wave propagation speed, but now it varies zonally. θ_o is determined by the initial perturbation, and x_o is the initial position of the perturbation. As shown by Eq. 8, the amplitude of the perturbations evolves during the propagation: $\theta \propto C_o^{-1/2}$, $h \propto \rho_o^{-1}C_o^{-1/2}$ and $u \propto C_o^{-3/2}$. Note that if $C_o(x)$ decreases during the eastward wave propagation, the amplitude of the perturbation increases, and the velocity amplitude increases faster than the buoyancy or height anomalies.

The previous solutions Eq. 8 are similar to the solutions obtained by Giese and Harrison (1990) in a different framework (see also (Benestad, 1997)).

3.2. Analytical solutions for density evolution in adiabatic conditions

To calculate the density perturbation created by the passage of the wave, we have to solve Eq. 6. For the adiabatic linear configuration considered in

249 this section, an approximation of this equation is:

$$\partial_t \rho = -u \partial_x \rho_o. \quad (10)$$

250 Using the solution for u given by Eq. 8, an approximate solution can be
 251 derived for the maximum density perturbation (see Appendix C), and we
 252 find that the structure of the maximum density anomaly created by the
 253 passage of the wave is:

$$\rho_{max} \propto -\frac{\rho'_o}{C_o^{3/2}} = -\frac{\rho'_o}{(-g\rho_o H_o / \rho_{ref})^{3/4}}. \quad (11)$$

254 3.3. Experimental setup in adiabatic conditions

255 We now analyze the propagation of an equatorial Kelvin wave in a setup
 256 representative of the initiation of El Nino events in the equatorial Pacific.
 257 We will compare and analyze results of the full nonlinear model from Eq.3-
 258 6 or consider the analytical solutions from Eq. 8-11. We consider two
 259 experiments that differ only by their equilibrium states, leading to either a
 260 CP or EP pattern of density anomalies.

261 First, for the EP experiment the equilibrium state is specified as:

$$\begin{aligned} U_o &\simeq 0, \\ H_o &= H_{mean} - \Delta H_{max} \frac{x - L/2}{L}, \\ \rho_o &= \rho_{mean} + \Delta \rho_{max}^{lin} \frac{x - L/2}{L}, \end{aligned} \quad (12)$$

262 where L is the basin width, H_{mean} is the mean mixed layer depth (reached
 263 in the middle of the domain) and ΔH_{max} its variation between the western
 264 and eastern sides, ρ_{mean} is the mean mixed layer density and $\Delta \rho_{max}$ its
 265 variation between the western and eastern sides. We set $L = 30.000 \text{ km}$,
 266 $H_{mean} = 120 \text{ m}$, $\Delta H_{max} = 160 \text{ m}$, $\rho_b = 0$, $\rho_{ref} = 1000 \text{ kg/m}^3$, $\rho_{mean} =$

267 -3.0 kg/m^3 , $\Delta\rho_{max}^{lin} = 3 \text{ kg/m}^3$. A large basin scale $L = 30.000 \text{ km}$ has
 268 been chosen so as to get rid of boundary effects at the western and eastern
 269 side of the basin. We concentrate our attention on what happens within the
 270 area $x \in [10.000, 25.000] \text{ km}$ (whose length $\Delta x = 15.000 \text{ km}$ is typical of
 271 the equatorial Pacific).

272 Second, for the CP experiment, we modify the mean density zonal vari-
 273 ation and set:

$$\rho_o = \rho_{mean} + \Delta\rho_{max}^{lin} \frac{x-L/2}{L} + \Delta\rho_{max}^{th} th((x - x_{th})/L_{th}). \quad (13)$$

274 where we have chosen $\Delta\rho_{max}^{lin} = 0.5 \text{ kg/m}^3$, $\Delta\rho_{max}^{th} = 3 \text{ kg/m}^3$ and $L_{th} =$
 275 5.000 km and $x_{th} = L/2$. Other fields retain the values specified above.
 276 Table D.3 in Appendix D summarizes all parameters used in the present
 277 study.

278 Figure 2 represents the variation of the wave propagation speed C_o for
 279 the EP and CP experiment. For both configurations, the wave propagation
 280 speed C_o decreases from 3 m/s to 0.8 m/s at the eastern side of the basin,
 281 with a mean propagation speed $C_o^{mean} \simeq 2 \text{ m/s}$, but notice the strong
 282 variation in the middle of the basin, associated with the density front for
 283 the CP experiment.

284 Finally, the initial perturbation is identical for both the EP and CP
 285 experiments:

$$\begin{aligned} h(t=0) &= h_o = \delta h_{max} \exp(-((x - x_o)/l_p)^2), \\ u(t=0) &= u_o = \frac{\sqrt{-\Theta_o}}{H_o} h_o, \\ \theta(t=0) &= \theta_o = \frac{\Theta_o}{H_o} h_o, \end{aligned} \quad (14)$$

286 where l_p is the perturbation lengthscale, x_o is the initial position of the per-
 287 turbation and δh_{max} the amplitude of the mixed layer depth anomaly. The

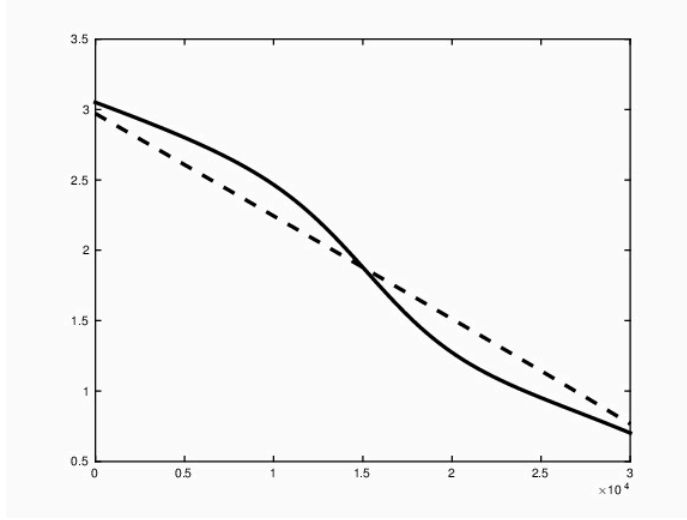


Figure 2: Gravity wave propagation speed C_o (in m/s) for the EP (dashed line) and CP (solid line) experiments as a function of the zonal coordinate x (in km). Note the variation in the middle of the basin for the CP.

288 velocity anomaly is here specified to obtain an eastward propagating gravity
 289 wave. θ_o is chosen so that the initial density perturbation is zero. Unless
 290 stated otherwise the initial position of the perturbation is $x_o = 10.000 \text{ km}$
 291 and its horizontal scale is $l_p = 2000 \text{ km}$. Its amplitude is $\delta h_{max} = 1 \text{ m}$,
 292 small enough that the perturbation propagates as an eastward linear wave.

293 3.4. Results for numerical experiments in adiabatic conditions

294 Figure 3 shows results for the EP experiment. We see the propagation of
 295 the gravity wave signal (u , h , θ fields) and the density perturbation created
 296 by the passage of the wave (here a pure advection of the density by the
 297 velocity perturbation) calculated by the numerical model. The numerical
 298 experiment (solving Eq. 3 and 4) is run for 150 days and on each plot
 299 we superimpose the signal structure every 10 days. The thick line on each
 300 plot is the analytical result (Eq. 8 and 11), giving the evolution of the
 301 maximum amplitude of the signal during the wave propagation. It is very
 302 close to the numerical results. Note that we have also plotted $-h$ instead of
 303 h so as to represent the variations of the position of the thermocline, often
 304 represented by the 20°C isotherm (and we thus define $\delta z_{20} = -h$). The
 305 wave is associated with a deepening of the thermocline, corresponding to a
 306 downwelling event.

307 The layer thickness, velocity and buoyancy propagate eastward with
 308 growing amplitude and the density perturbations monotonically increase
 309 eastward during the propagation of the wave, generating an EP type El
 310 Niño.

311 Figure 4 shows results for the CP experiment. Again the analytical re-
 312 sults are close to the numerical ones, but in this case, the maximum density
 313 anomaly is reached in the middle of the basin (in the region of the back-

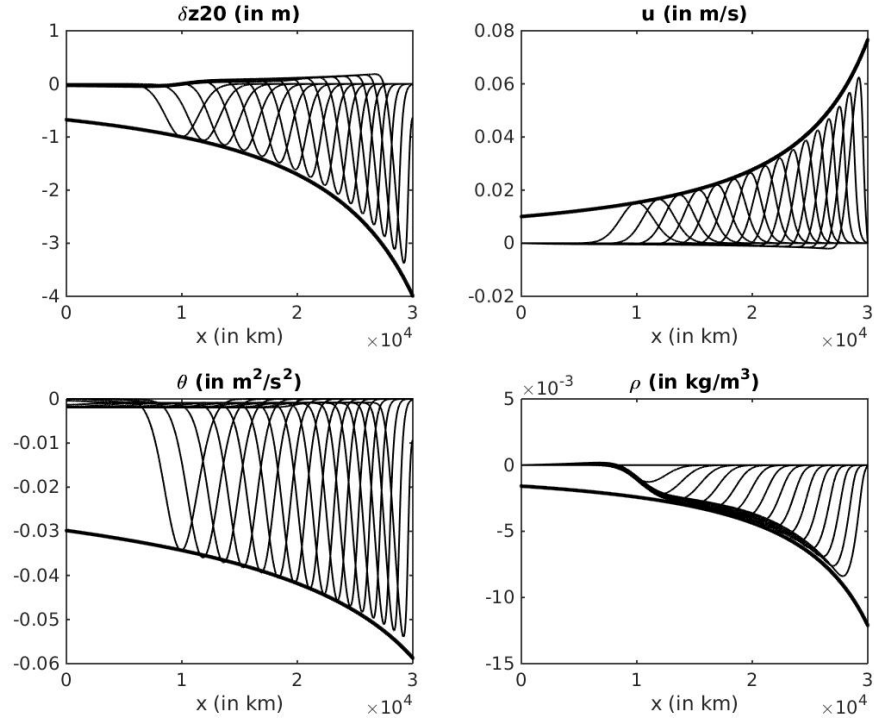


Figure 3: Evolution of the thermocline position $\delta z_{20} = -h$ representing the thermocline variations (top left), velocity anomaly (top right), θ (bottom left) and density anomaly (bottom right) for the EP experiment in adiabatic conditions for 150 days. In each panel, we superimpose the field output every 10 days. The solid thick curve indicates the analytical solution for the maximum perturbation created by the wave. The wave induces a downwelling and the creation of a negative density anomaly (or positive temperature anomaly).

ground front), generating a CP type signal. Also note that the gravity wave signal (u , h , θ fields) exhibit the same behaviour as before, with a monotonic increase of the wave amplitude at a rate that is almost twice the previous one.

3.5. Physical analysis for adiabatic conditions

To analyze the circumstances in which EP or CP types are reached, we discuss the analytical derivative of the density anomaly ρ'_{max} (see Eq. 11):

$$\rho'_{max} \propto -\rho''_o + \frac{3}{4}\rho'_o\left(\frac{\rho'_o}{\rho_o} + \frac{H'_o}{H_o}\right). \quad (15)$$

For a CP type, the density anomaly reaches a maximum in the middle of the basin, so we must get $\rho'_{max} = 0$ within the basin during the propagation.

For a configuration representative of the equatorial Pacific, the second term on the right hand side is always negative (the layer depth decreases $H'_o < 0$, the mixed layer density anomaly increases $\rho'_o > 0$ from West to East but $\rho_o < 0$). Thus, if ρ''_o is small, the perturbation of the density field monotonically increases eastward, yielding a structure for the density perturbation of the EP-type El Niño, as is the case in Fig. 3. To reach a CP type structure, ρ''_o must be positive and sufficiently strong somewhere along the equator, a condition that requires a density front for the equilibrium state.

To conclude, for adiabatic evolution, the wave propagation is associated with a purely advective effect on the density field, and the physics is quite simple: the generation of EP or CP type only depends on the background stratification characteristics. The stronger the density gradient, the stronger the density anomaly created by a given velocity perturbation. Frontal regions are thus naturally subject to strong local anomaly generation and CP

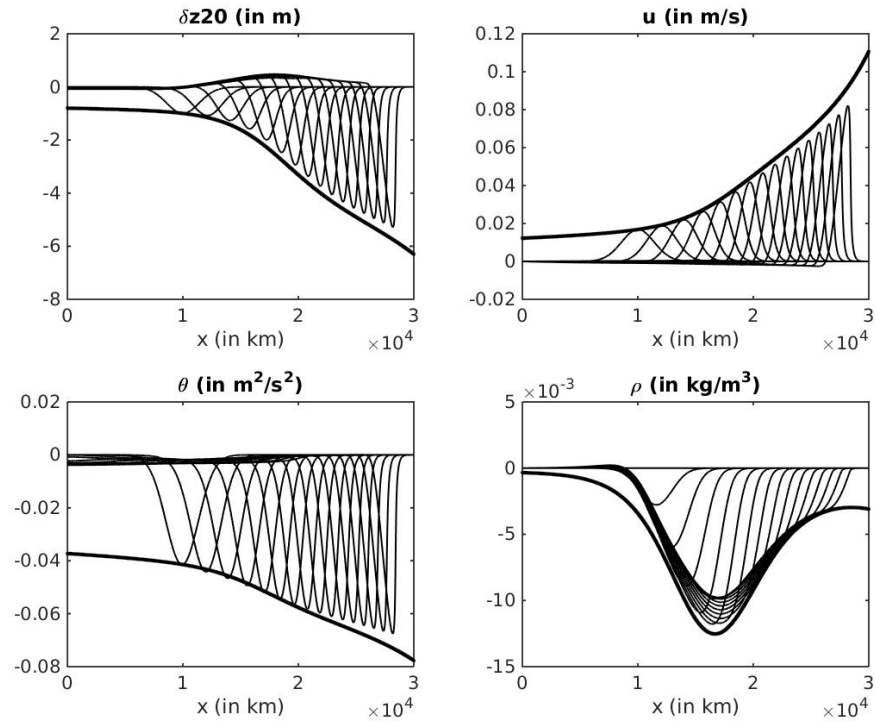


Figure 4: Same as Fig. 3 for the CP experiment.

type structures. Note however that, away from the front, the perturbation amplitude continues to grow because of the decay of the background stratification. If this amplification process is strong enough, it is also possible to have a local maximum of the density anomaly (CP structure) followed by further amplification of the perturbation which reaches another local maximum near the coast.

4. Results for linear waves in diabatic conditions

4.1. Parameterization of the forcing terms

We now evaluate the influence of possible diabatic effects on the numerical and analytical results. For this, we repeat the EP and CP experiments presented in the previous section, but with diabatic forcing terms. If at equilibrium the latter are determined by the physical fields (see Eq. 4), in the general case they can be modified during the wave propagation. Two kinds of modifications can occur:

1. retroactive effects, due to ocean/atmosphere coupling and to the modification of the ocean forcings by the perturbations due to the gravity wave. For instance the modification of H during the passage of the wave induces a modification of the wind stress forcing term;
2. external effects, associated with processes that have no link with the perturbations due to the gravity wave, and which can be considered as stochastic effects (e.g. stochastic wind bursts).

We only consider retroactive effects, which arise when forcing terms depend on the mixed layer characteristics. The variation of the forcing terms

361 can then be written:

$$\begin{aligned}\delta F^U &= F(U_o + u, H_o + h, \Theta_o + \theta) - F_o(U_o, H_o, \Theta_o) \\ &\simeq \frac{\partial}{\partial U} F_o \cdot u + \frac{\partial}{\partial H} F_o \cdot h + \frac{\partial}{\partial \Theta} F_o \cdot \theta.\end{aligned}\quad (16)$$

362 Taking into account that in the case of gravity waves u , h and θ are propor-
363 tional (see Eq. 7), we can write the forcing terms as Newtonian cooling for
364 the perturbation evolution:

$$\begin{aligned}\delta F^U &= -\alpha^U u, \\ \delta F^H &= -\alpha^H h, \\ \delta F^\Theta &= -\alpha^\Theta \theta.\end{aligned}\quad (17)$$

365 where the α values can thus be evaluated from existing parameterizations.

366 Note that more general parameterizations of the forcing terms including
367 delocalized effects (e.g. a wind response located west of the density pertur-
368 bations) are in principle possible but are beyond the scope of the present
369 study.

370 4.2. Analytical solutions for the wave signal in diabatic conditions

371 The analytical solutions obtained under adiabatic conditions in section
372 3 can be extended to take into account Newtonian cooling diabatic terms
373 Eq. 17. We get (see Appendix B):

$$\begin{aligned}\theta &= \frac{C_o(x = x_o)^{1/2}}{C_o(x)^{1/2}} e^{-(\alpha^\Theta + \alpha^U)x/2C_o} \theta_o(x/C(x) - t), \\ u &= \frac{\theta}{C_o(x)} = \frac{C_o(x = x_o)^{1/2}}{C_o(x)^{3/2}} e^{-(\alpha^\Theta + \alpha^U)x/2C_o} \theta_o(x/C(x) - t) \\ h &= \frac{\rho_{ref}\theta}{g\rho_o(x)} = \frac{\rho_{ref}C_o(x = x_o)^{1/2}}{g\rho_o(x)C_o(x)^{1/2}} e^{-(\alpha^\Theta + \alpha^U)x/2C_o} \theta_o(x/C(x) - t)\end{aligned}\quad (18)$$

374 4.3. Analytical solutions for the density evolution in diabatic conditions

375 When taking into account diabatic terms, it is interesting to general-
 376 ize the density evolution Eq. 6 and consider a damping term specifically
 377 depending on the surface density, leading to

$$\partial_t \rho_s + U \partial_x \rho_s = \frac{\rho_{ref}}{gH} F^\Theta - \frac{\rho_s}{H} F^H + F^\rho(\rho_s). \quad (19)$$

378 The additional term F^ρ in the density equation plays a minor role and can
 379 be neglected for the physics associated with the propagating wave (Eq. 18
 380 remain valid), but it is important for the density evolution itself. As already
 381 used above, we consider a small perturbation and linearize the function
 382 $F^\rho(\rho_s)$ to give

$$\delta F^\rho = -\alpha^\rho \rho. \quad (20)$$

383 Using Eq. 4, 17 and the existing relationship between u , h , θ for the
 384 wave signal (Eq. 18) yields the following linearized evolution equation for
 385 the surface density perturbation $\rho = \rho_s - \rho_o$ (see Appendix C):

$$\partial_t \rho = -u \partial_x \rho_o + \frac{\rho_{ref}(\alpha^H - \alpha^\Theta)}{g H_o} \theta - \alpha^\rho \rho. \quad (21)$$

386 A new approximate solution is then derived (see Appendix C) for the max-
 387 imum density perturbation:

$$\rho_{max} \propto \left[-\frac{\rho'_o}{C_o^{3/2}} + \frac{\rho_{ref}(\alpha_o^H - \alpha_o^\Theta)}{g H_o C_o^{1/2}} \right] e^{-(\alpha^\Theta + \alpha^U)x/2C(x)} e^{-\alpha^\rho l_p/C_o(x)}. \quad (22)$$

388 This analytical solution looks quite complicated, but, as we will show, re-
 389 mains reasonably accurate. Notice that the α terms can either limit the
 390 generated density anomaly amplitude or increase it. In particular, the dif-
 391 ference $\alpha^H - \alpha^\Theta$ determines the net effect ($\alpha^H - \alpha^\Theta < 0$ is associated with
 392 damping).

Eq. 22 gives an analytical estimate of the maximum density perturbation generated by the passage of the gravity wave. At a given location, it is valid during the passage of the wave, but the $-\alpha^\rho \rho$ term continues to act after the passage of the wave: if $\alpha^\rho > 0$ the density anomaly is then damped at a rate $e^{-\alpha^\rho t}$.

4.4. Validation of the analytical solutions in diabatic conditions

There are additional approximations in the derivation of the analytical solutions with diabatic terms (Eq. 18 and 22), but the solutions still remain quite accurate. We have indeed, tried many different combinations for α^U , α^H , α^Θ , α^ρ and have always found that the analytical predictions remained close to the numerical results (Eq. 3, 4, 17 and 20).

To illustrate this, we here resume the EP experiments (see Fig. 3), but with $\alpha^U = \alpha_o$, $\alpha^H = 0$, $\alpha^\Theta = 0$ and $\alpha^\rho = 0$, where $\alpha_o = 1/50 \text{ days}^{-1} = 2.3 \cdot 10^{-7} \text{ s}^{-1}$ is a typical damping rate (as we will see below, this value corresponds to a threshold for the influence of diabatic effects). The numerical and analytical results are represented in Fig. 5. Note the analytical solution indeed gives good results. As can be expected, the velocity, buoyancy and layer depth anomalies are all damped in comparison with the adiabatic solution. The maximum density anomaly remains nearly constant during the eastward propagation. If α^U is further increased, the maximum density anomaly is reached close to the generation area and becomes of CP type (not shown).

Many other experiments have been performed and confirm the good agreement between the analytical and numerical model, even using complicated equilibrium states. To illustrate this, Fig. 6 shows the results for the CP configuration (see Fig. 4), but choosing $\alpha^U = \alpha^\rho = 0$, $\alpha^H = 0.3 \alpha_o$

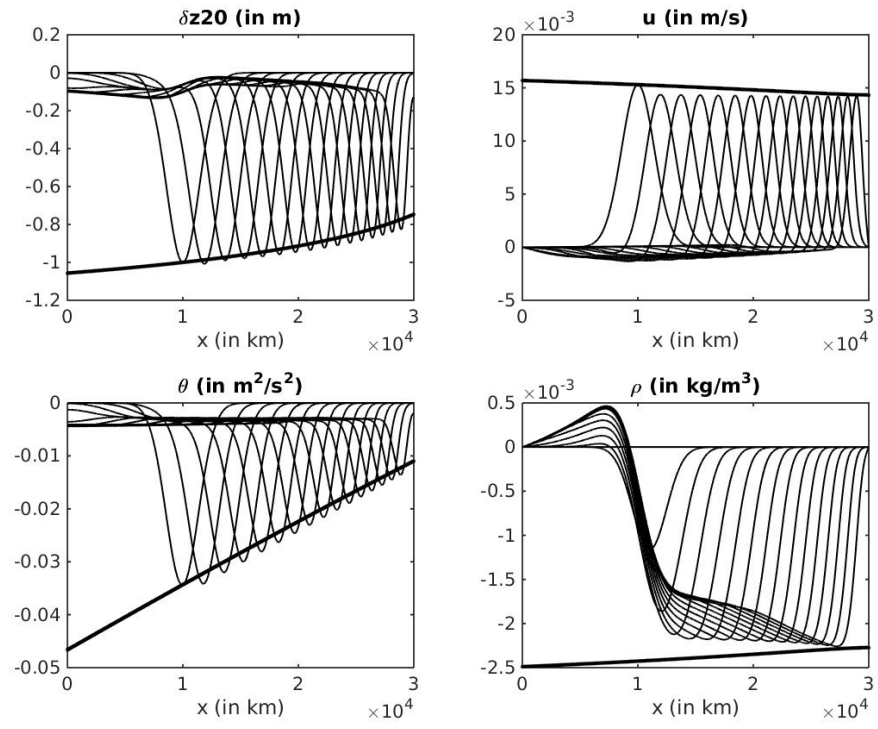


Figure 5: EP experiment with diabatic forcings ($\alpha^U = \alpha_o$, $\alpha^H = 0$, $\alpha^\Theta = 0$, $\alpha^\rho = 0$). The graph shows the same fields as Fig. 3.

419 and $\alpha^\Theta = -0.3 \alpha_o$. The choice for the parameter is arbitrary (in particular
 420 we have chosen $\alpha^\Theta < 0$, meaning that the buoyancy anomaly is increased
 421 by retroactive effects of the forcing terms), but it underlines the fact that
 422 diabatic effects can also modify the structure of the density anomaly from
 423 CP to EP type.

424 To conclude, if strong enough, diabatic terms coming from retroactive
 425 effects can considerably modify the type and strength of the density anomaly
 426 generated by the wave during its propagation. The analytical solutions are
 427 able to determine under which conditions (equilibrium state and damping
 428 vs amplification rates) this is achieved.

429 **5. Sensitivity analysis**

430 *5.1. Influence of the perturbation amplitude*

431 When the initial wave amplitude is larger, non-linear effects can modify
 432 the previous results. We here resume the reference adiabatic experiments
 433 (section 3.3), but with $\delta h_{max} = 20 \text{ m}$ (cf Eq. 14), which is a typical initial
 434 amplitude observed in the Pacific during El Niño events. This value leads to
 435 strong non-linearities as shown in Fig. 7 for the EP and Fig. 8 for the CP
 436 configurations. Note that in both configuration, the wave propagates faster
 437 and a shock is created (corresponding to the breaking of the gravity wave)
 438 whose effect is to damp the perturbation amplitude. The velocity anomaly
 439 is halved in comparison with the expected linear value given by the analytic
 440 solution. The maximum density anomaly however remains quite close to the
 441 analytical prediction. Even though we have recorded a significant decrease
 442 (about 30 %) with other choices for the background characteristics H_o and
 443 ρ_o , the analytical model seems able to predict the density anomaly, even in

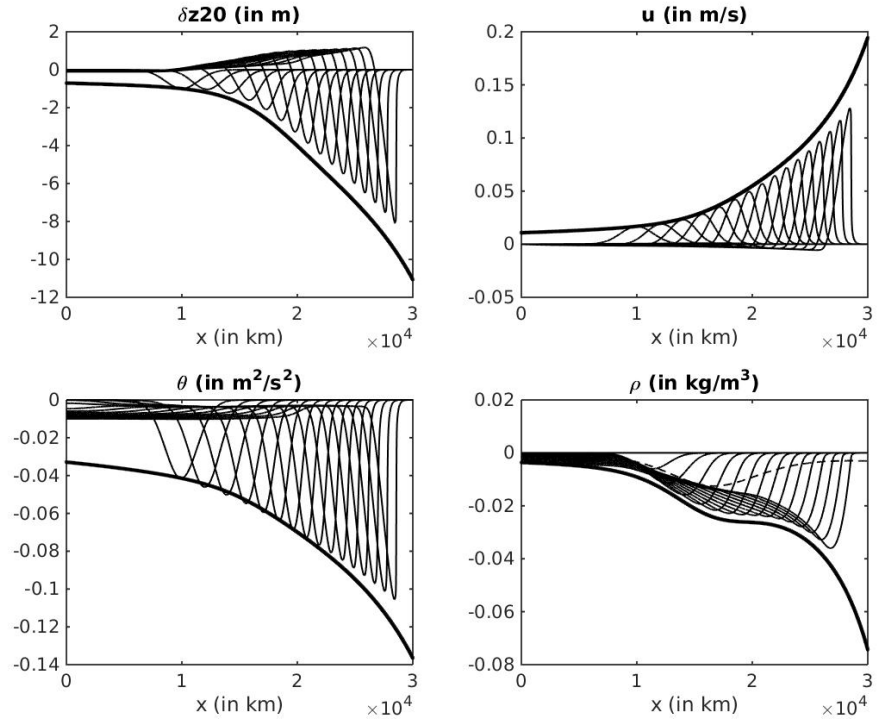


Figure 6: CP experiment with diabatic forcings ($\alpha^U = \alpha^\rho = 0$, $\alpha^H = 0.3 \alpha_o$ and $\alpha^\Theta = -0.3 \alpha_o$). The graph shows the same fields as Fig. 4. Note the similarity with Fig. 4 for the shape of the propagating anomalies, but the strong modification for the maximum density anomaly (the dashed line on the density plot represents the analytical solution valid without forcings).

444 finite amplitude, non-linear regimes.

445 As far as the amplitude of the density perturbation is concerned, note
446 that a density anomaly of $\delta\rho_{max} = -1 \text{ kg/m}^3$ roughly corresponds to an
447 anomaly of $4 \text{ }^\circ\text{C}$ and is thus taken as the order of magnitude representing
448 strong impact. In the present case, the maximum anomaly reaches $\delta\rho_{max} =$
449 -0.25 kg/m^3 and remains modest. This is further accentuated by non-
450 linear effects as they generate damping of the wave in comparison with the
451 linear theory. It thus appears that, to reach significant density anomalies,
452 amplifying retroactive effects are necessary. Nevertheless, the conclusions on
453 the localization of density anomalies from section 3 and 4 remain valid: in
454 the present simplified configuration, nonlinearities do not modify the EP/CP
455 patterns.

456 5.2. Influence of diabatic retroactive effects

457 We now estimate when retroactive effects, associated with the New-
458 tonian cooling terms and the damping rates α , have a significant effect
459 on the structure (CP v.s. EP) and strength of the density anomaly gen-
460 erated by the wave. We thus use Eq. 22 to analyze the sensitivity of
461 the density anomaly structure to the configuration parameters, in partic-
462 ular the damping rates. Fig. 9 shows the results for the EP configu-
463 ration (see section 3.3 and Fig. 3 for the $\alpha = 0$ adiabatic case) where
464 we have set $\delta h_{max} = 20 \text{ m}$, $\alpha^\rho = 0$ and $\alpha^H = \alpha^U = \alpha^\Theta = \alpha$, where
465 $\alpha \in [-2\alpha_o, +2\alpha_o]$ ($\alpha_o = 1/50 \text{ days}^{-1} = 2.3 \cdot 10^{-7} \text{ s}^{-1}$). For this
466 choice, the structure of the density anomaly is of the EP type until retroac-
467 tive processes are strongly damping. Indeed, when $\alpha > 0.5 \alpha_o$ the rate of
468 decrease is strong enough to counteract the amplifying effect of the modi-
469 fication of the stratification and the initial perturbation decreases. In this

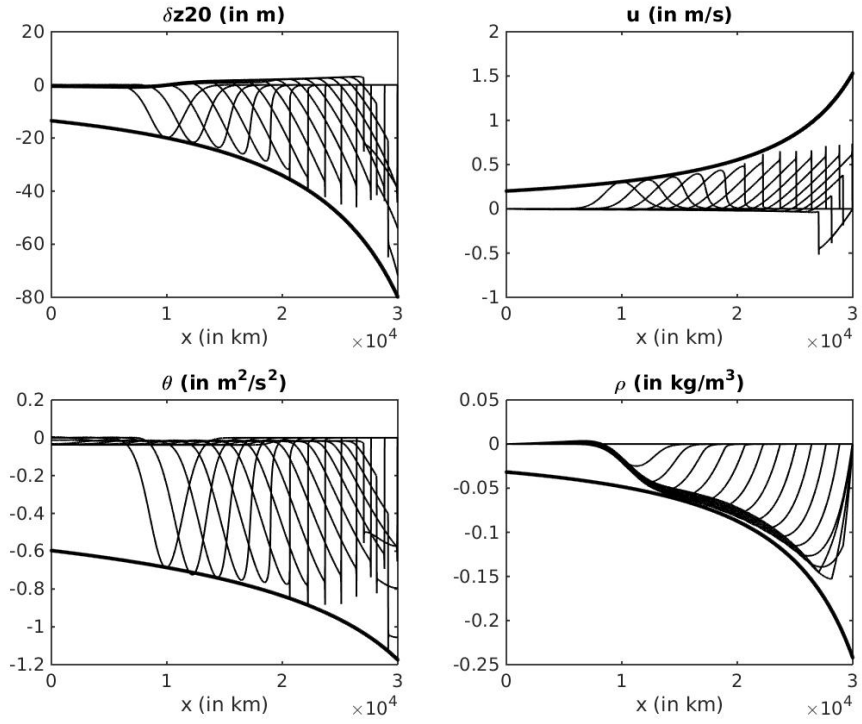


Figure 7: Same EP configuration as Fig. 3 except for $\delta h_{max} = 20$ m. Evolution of the layer depth anomaly (top left), velocity anomaly (top right), θ (bottom left) and density anomaly (bottom right) for 150 days with an output every 10 days. For each field, the solid thick curve indicates the analytical solution for the maximum perturbation created by the wave.

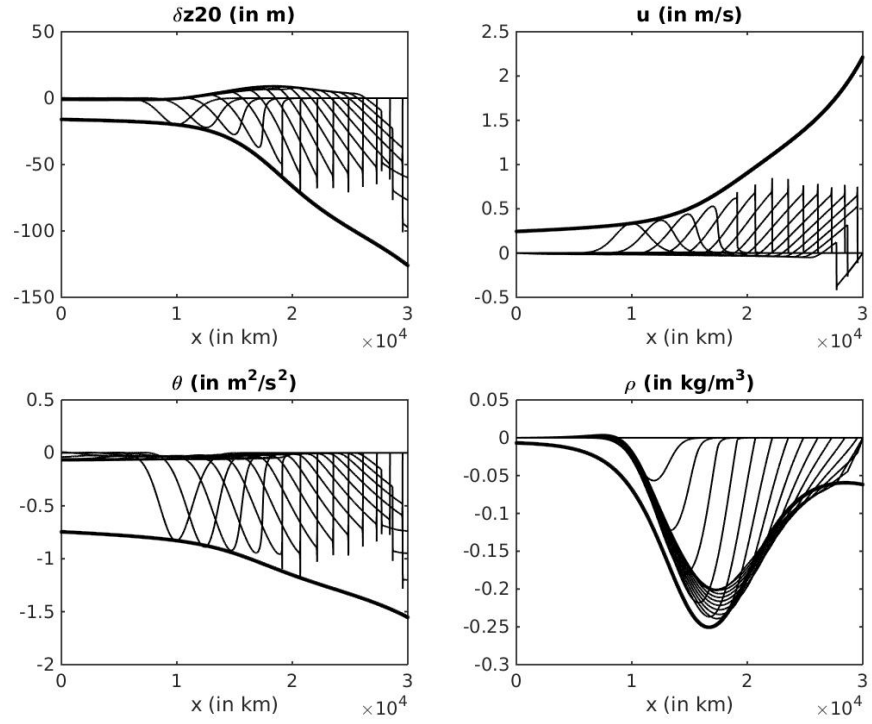


Figure 8: Same CP configuration as Fig. 4 except for $\delta h_{max} = 20$ m. Evolution of the layer depth anomaly (top left), velocity anomaly (top right), θ (bottom left) and density anomaly (bottom right) for 150 days with an output every 10 days. For each field, the solid thick curve indicates the analytical solution for the maximum perturbation created by the wave.

case the structure becomes CP, but note that the maximum perturbation values does not exceed $\delta\rho_{max} = -0.05 \text{ kg/m}^3$ (for $\alpha \in [0.5\alpha_o, 2\alpha_o]$), which is weak, even for CP El Niño events. When the evolution corresponds to EP type ($\alpha < 0.5 \alpha_o$), the maximum values reached at the eastern coast remain modest ($\delta\rho_{max} < -0.2 \text{ kg/m}^3$ for $\alpha = 0$ for instance) unless the retroactive processes are strongly amplifying: $\delta\rho_{max} < -1 \text{ kg/m}^3$ for $\alpha = -0.5\alpha_o$.

Fig. 10 shows the results for the CP configuration (see section 3.3 and Fig. 4 for the $\alpha = 0$ adiabatic case), where we have again set $\delta h_{max} = 20 \text{ m}$, $\alpha^\rho = 0$ and $\alpha^H = \alpha^U = \alpha^\Theta = \alpha$, where $\alpha \in [-2\alpha_o, +2\alpha_o]$. For damping situations ($\alpha \in [0, 2\alpha_o]$), the structure remains of the CP type and the maximum density perturbation range is $\delta\rho_{max} \in [-0.2, -0.1] \text{ kg/m}^3$. Again, amplifying retroaction is necessary to reach strong enough density anomalies ($\delta\rho_{max} < -0.4 \text{ kg/m}^3$ when $\alpha < -0.5\alpha_o$). When $\alpha < -0.6\alpha_o$, the structure becomes EP, but for strongly negative α , the amplitude of the density perturbation becomes unrealistically low : $\delta\rho_{max} < -2 \text{ kg/m}^3$ for $\alpha < -\alpha_o$.

Changing the relationship between α^ρ , α^H , α^U and α^Θ can modify the previous results qualitatively and quantitatively. We have tested several options and our results show that some general conclusion associated with the two previous configurations are robust:

- some amplifying retroaction (α negative for some or all physical fields) is necessary to reach significant density (temperature) anomalies with a single wave (the case of multiple waves is addressed below);
- to reach a significant CP El Niño, the initial stratification plays a major role: the preexistence of a density front in the background stratification is necessary.

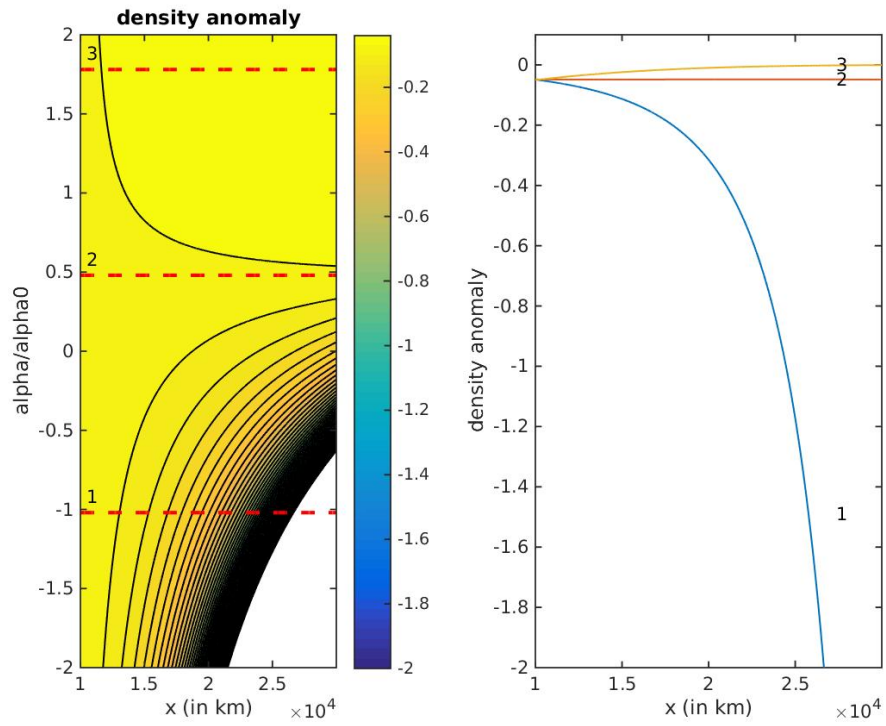


Figure 9: Left panel: density anomaly structure as a function of the zonal coordinate x (in km) and the damping rate α for the EP configuration (see section 3.3 and Fig. 3). Right panel: density anomaly structure as a function of the zonal coordinate x (in km) for selected damping coefficients (corresponding to the red dashed lines on the left panel). Note the transition from EP (1) to CP (3) and the intermediate structure with a flat density variation (2).

496 The evaluation of realistic ranges for the value of α can be determined
 497 from basic parameterizations of forcings and diabatic processes (see Barnier
 498 (1998) for a review). This is however beyond the scope of the present work
 499 and is left for a future study.

500 5.3. *Effect of the perturbation scale*

501 We here vary the initial perturbation scale l_p from 1000 km to 6000 km
 502 (cf Eq. 14, $l_p = 2000$ km in all previous experiment). All damping rates are
 503 set to zero and we calculate the density anomaly for both the EP (see Fig.
 504 3) and CP (see Fig. 4) configurations but with $\delta h_{max} = 20$ m. As can be ex-
 505 pected, the larger the perturbation scale, the stronger the maximum density
 506 anomaly and of course the wider the area where strong density anomalies
 507 are created. The structure (EP or CP) of the perturbation is not modified
 508 and we notice that the maximum density anomalies remain modest unless
 509 l_p becomes very large: $\delta \rho_{max} < -0.7$ kg/m³ for $l_p > 6000$ km. We thus
 510 believe that varying the initial perturbation scale is not enough to reach the
 511 values associated with the strongest El Niño events and that, as already un-
 512 derlined above, multiple waves or significant amplifying retroaction effects
 513 are necessary.

514 5.4. *Effect of the background circulation*

515 The effect of the background circulation U_o was set to zero in all previous
 516 analytical and numerical results. We were not able to find a solution when
 517 $U_o \neq 0$ with our analytical framework, but we have evaluated the effect of
 518 a background shear using the numerical simulations. We have chosen :

$$U_o(x) = U_{max} 0.5 (1 - \cos(\frac{2\pi}{L} x)), \quad (23)$$

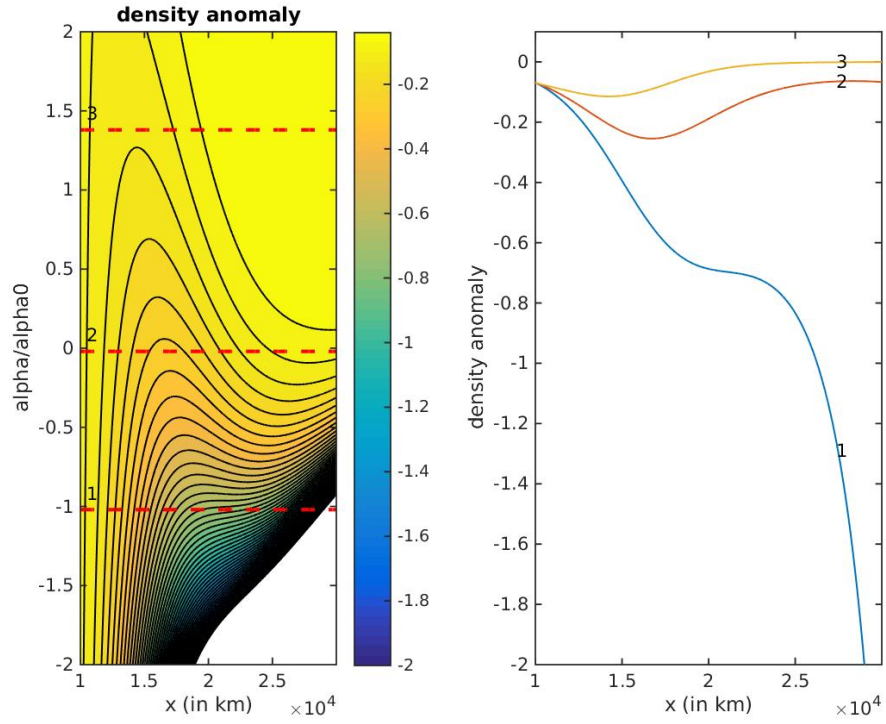


Figure 10: Left panel: density anomaly structure as a function of the zonal coordinate x (in km) and the damping rate α for the CP configuration (see section 3.3 and Fig. 4). Right panel: density anomaly structure as a function of the zonal coordinate x (in km) for selected damping coefficients (corresponding to the red dashed lines on the left panel). Note the transition from CP (2 and 3) to EP (1).

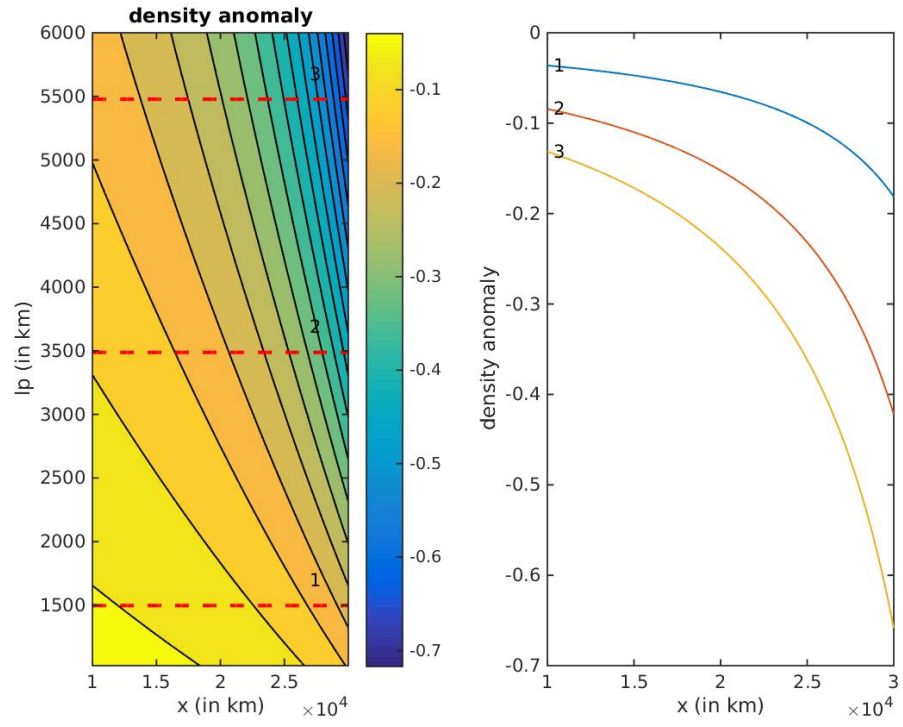


Figure 11: Left panel: density anomaly structure as a function of the zonal coordinate x (in km) and the initial -Gaussian- perturbation scale l_p for the EP configuration (see section 3.3 and Fig. 3). Right panel: density anomaly structure as a function of the zonal coordinate x (in km) for selected lengthscales (corresponding to the red dashed lines on the left panel). Note the structure remains EP but the density anomaly increases with the perturbation lengthscale.

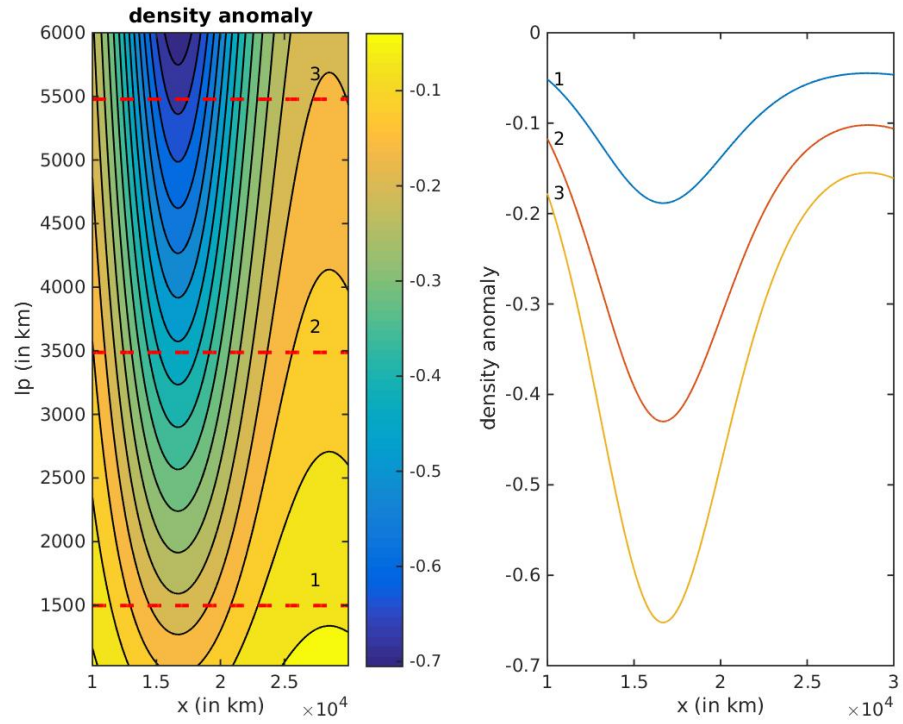


Figure 12: Left panel: density anomaly structure as a function of the zonal coordinate x (in km) and the initial -Gaussian- perturbation scale l_p for the CP configuration (see section 3.3 and Fig. 4). Right panel: density anomaly structure as a function of the zonal coordinate x (in km) for selected lengthscales (corresponding to the red dashed lines on the left panel). Note the structure remains CP but the density anomaly increases with the perturbation lengthscale.

519 so that U_o satisfies the closed boundary conditions at $x = 0$ and $x = L$ (ex-
520 tension of the domain). U_{max} is the maximum background velocity, reached
521 at the center of the domain.

522 We have repeated the reference EP and CP experiments, but with a
523 background velocity. The density evolution pattern is modified by the addi-
524 tional advection, but we have found that our previous results remain valid
525 as long as the maximum background velocity $U_{max} \in [-0.5 \text{ m/s}, 0.5 \text{ m/s}]$.
526 Observations indicate that the mean velocities along the equator are in this
527 range (see Picaut et al., 1997). In fact, the WKB approximation (see Gill
528 (1982), chapter 8)) shows that, if the background velocity gradient is small,
529 the evolution of a perturbation (in particular its amplitude) is not mod-
530 ified by the background current. There is just a shift in the wave group
531 velocity: $C_g^U = C_g^{U=0} + U$. However, special attention must be paid to
532 the density anomaly since it is not a wave propagation signal. Also, note
533 that since $F^H \neq 0$ (see Eq. 4), there exists a diabatic term in the density
534 anomaly evolution equation (see Eq. 6), and for a westward background
535 flow ($U_{max} < 0$) the density anomaly is now damped on the eastern side
536 and amplified on the western side. Adding damping effects probably also
537 complicates the physics. Further studies are obviously needed to evaluate
538 the limits and compare with realistic fields.

539 6. Effect of multiple waves: from CP to EP El Niño

540 It is interesting to note that in the CP configuration, in the presence of
541 a background density front, the effect of the wave is to smooth the front.
542 Figure 13a shows the evolution of the total upper layer density ρ_s for the CP
543 case and $\delta h_{max} = 20 \text{ m}$ (same experiment as in Fig. 8) and clearly shows

the smoothing effect. We may thus wonder if multiple waves on an initially CP configuration could eventually yield a structure that would favor an EP configuration.

To test this idea, we have used the numerical model with a specific background condition. The basin scale has been reduced to $L = 17.000 \text{ km}$ (representative of the equatorial Pacific zonal length) and the background density structure is given by Eq. 13 with $\Delta\rho_{max}^{lin} = 2.5 \text{ kg/m}^3$, $\Delta\rho_{max}^{th} = 1 \text{ kg/m}^3$ and $L_{th} = 1.000 \text{ km}$, and the front position is located at $x_{th} = 3.000 \text{ km}$. The background mixed layer depth structure has also been modified, and we have chosen:

$$H_o = H_{mean} - \Delta H_{max} \frac{x-L/2}{L} - \Delta H_{max}^{th} \tanh((x - x_{th})/L_{th}). \quad (24)$$

with $H_{mean} = 115 \text{ m}$, $\Delta H_{max} = 70 \text{ m}$ and $\Delta H_{max}^{th} = 30$. The initial perturbation located at the western coast ($x_o = 0 \text{ km}$), its extension is $l_p = 3000 \text{ km}$ and $h_{max} = 20 \text{ m}$. Six waves of this type are generated (one per month for 6 months). The boundary conditions have been arranged so that the wave is radiated (no amplification by bouncing at the eastern boundary). Finally, the damping rates have been set to zero, except for $\alpha^\rho = 0.15\alpha_o \simeq 3.5 \cdot 10^{-8} \text{ s}^{-1}$ (corresponding to a damping time scale of about one year). Figure 13b-c shows the evolution of the mixed layer density and height anomalies for 300 days. Note the displacement of the maximum density anomaly, from the center of the basin for the first waves to the eastern coast for the last wave. The strength of the density anomaly also reaches $\delta\rho_{max} \simeq -1 \text{ kg/m}^3$, which is the typical value of a strong El Niño event. This result illustrates the possibility of progression from CP to EP El Niño.

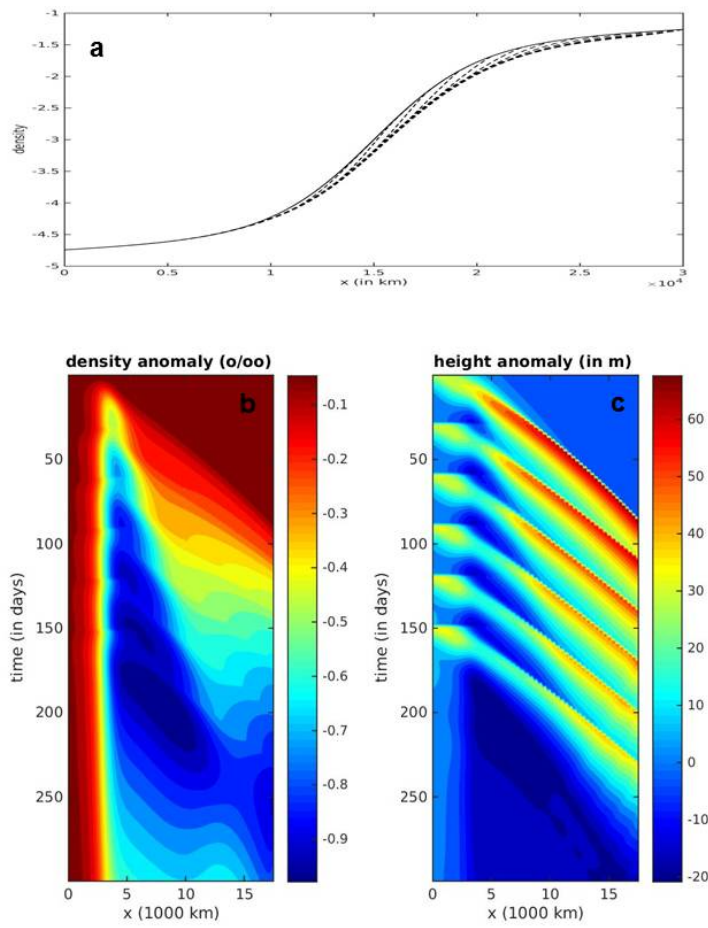


Figure 13: (a) Evolution of the total upper layer density structure for a 150 days with an output every 10 days (initial state in plain, evolution in dashed lines). Evolution of the density structure (b) and mixed layer depth (c) for 300 days for a simulation with multiple equatorial waves (6 waves launched every month for 6 months).

568 7. Discussion

569 In the present work, our goal was to understand the mechanisms leading
570 to the localization of El Niño events either in the Central (CP) or East-
571 ern Pacific (EP) and their continuity. We have thus presented a simplified
572 model to study the effect of equatorial Kelvin waves on the generation of
573 density (temperature) anomalies. We considered the evolution of a reduced
574 gravity, mixed layer along the equator and the equations are thus 1D. Ap-
575 proximate analytical solutions have been found for linear waves propagat-
576 ing in a spatially variable background stratification, maintained by diabatic
577 forcings. Damping/amplifying effects, associated with retroactive processes,
578 have been taken into account in the form of Newtonian cooling terms. The
579 non-linear equations have been solved numerically to validate the theoretical
580 results.

581 We have first studied adiabatic cases for which there is no feedback of the
582 perturbation of the wave on the forcings (section 3). In this case the density
583 (or temperature) field is purely advected by velocity perturbation associated
584 with the wave during its passage. The final density anomaly depends on the
585 amplitude of the displacement and on the local density gradient. Its shape
586 is given by Eq. 11.

587 Figure 14 schematizes the evolution of the wave and temperature field
588 in this adiabatic case (here we have used temperature instead of density for
589 easier connection with the usual ENSO description). The propagation speed
590 of the Kelvin wave diminishes eastward (blue arrows) so the perturbation
591 height (dashed blue lines) and velocity (red arrows) increase eastward lead-
592 ing to greater displacement of isotherms (vertical red lines) and stronger
593 anomaly at the Eastern boundary. This process favors EP events (Fig. 14,

left column). Strong local density gradients, associated with fronts, generate strong local anomalies. Fronts are also associated with local deceleration of the wave propagation, leading to stronger local amplification of the wave perturbation (height and velocity). Both processes favor the generation of stronger density anomalies in the vicinity of the initial front, corresponding to a CP event (Fig. 14, right column).

600

In this adiabatic case, the existence of a front is thus a prerequisite to getting a CP structure. However, as shown by Eq. 11 and 15 and schematized in Fig. 14, the type of the final structure depends on details of the initial stratification. There thus exists a continuity between CP and EP events whose occurrence depends on the shape of the background surface density or layer depth. Table 1 indicates how several parameters influence the structure type if all other parameters are kept constant. For instance, according to our results, a shallower mean upper layer depth (diminishing $\overline{H_o}$) or a stronger difference between western and eastern upper layer depths ($\partial_x H_o$ becomes "more negative") favors EP structures. Conversely, increasing the mean upper layer temperature (so that the mean density $\overline{\rho_o}$ becomes "more negative") or a weaker difference between western and eastern upper layer temperature (so that $\partial_x \rho_o$ becomes closer to 0) favors CP structures. These rules have to be used cautiously as in practice the parameters discussed in table 1 do not evolve independently.

It has also been shown that retroactive effects, associated with damping or amplification of the wave perturbations, or a succession of multiple waves are also important factors influencing the fate of an ENSO. Again table 1 summarizes the influence of these parameters. Amplifying feedbacks favor EP, and it is possible to change a CP event into a EP event, provided am-

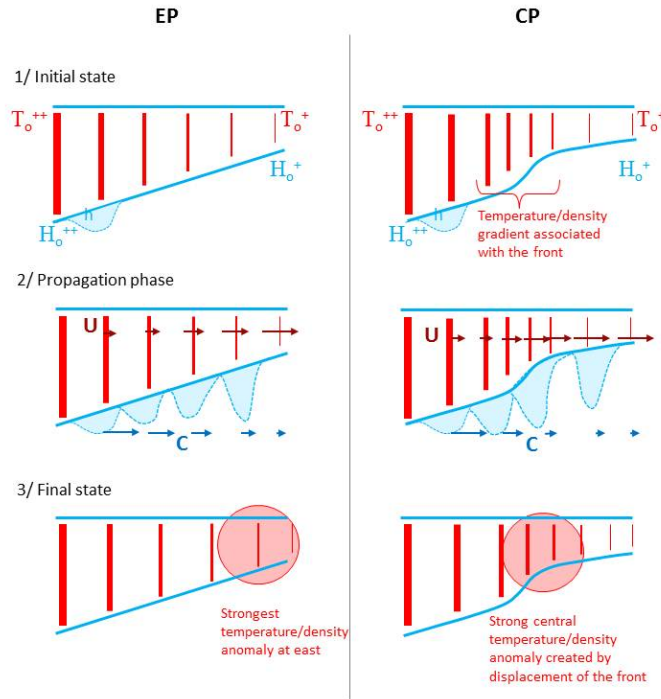


Figure 14: Schematic vertical sections illustrating the impact of a Kelvin wave on the upper-layer temperature field along the equator, in adiabatic conditions. Thick blue lines denote the surface and base of the layer, thin dashed lines denote the layer thickness perturbation associated with the Kelvin wave, whose propagation speed diminishes eastward (blue arrows). The dark red arrows show the Kelvin wave current perturbation and increase eastward. The red vertical lines correspond to isotherms, the thicker the line, the higher the temperature. The temperature field is purely advected by the velocity perturbation due to the Kelvin wave. The final anomaly depends on the displacement amplitude and on the initial local gradient of temperature. The strongest anomaly can be reached at the center (corresponding to a CP event) if there is a temperature front (right column).

Parameters/values		small		high	
$-\partial_{x2} \rho_o$ (<i>front</i>)		(0)	EP		CP (+ ∞)
H_o	$\overline{H_o}$ (<i>mean value</i>)	(0)	EP		CP (+ ∞)
	$\partial_x H_o$	($-\infty$)	EP		CP (0)
ρ_o	$\overline{\rho_o}$ (<i>mean value</i>)	($-\infty$)	CP		EP (0)
	$\partial_x \rho_o$	(0)	CP		EP (+ ∞)
Number of waves		(1)	EP		EP (+ ∞)
		(1)	CP		EP (+ ∞)
α		($-\infty$) EP	EP (<0)	Weak influence	(>0) EP CP (+ ∞)
		($-\infty$) EP	CP (<0)		(>0) CP CP (+ ∞)

Table 1: Diagram indicating how parameters influence the structure type (CP or EP). The important parameters are $\partial_{x2} \rho_o$ (indicating the strength of the density front), the mean values and gradients of the upper layer depth and density ($\overline{H_o}$, $\partial_x H_o$, $\overline{\rho_o}$, $\partial_x \rho_o$), the number of successive Kelvin waves and the effect of diabatic feedbacks, parameterized as Newtonian cooling terms α ($\alpha < 0$ corresponds to amplifying feedbacks, $\alpha > 0$ to damping). The specific range of evolution (small values to high values) for each parameter is given in parenthesis.

621 plification is strong enough. Damping feedbacks favor CP structures, and
622 it is possible to transform an EP into a CP structure with strong enough
623 damping. The thresholds beyond which the density structure is strongly
624 modified, as a function of all parameters can be evaluated using our ana-
625 lytical results. The number of waves does not modify the fate of an EP
626 event but can transform an initially CP into an EP event. This result is
627 consistent with observations that have shown that multiple westerly wind
628 bursts are necessary to get an EP El Niño (see Menkes et al., 2014). The
629 number of equatorial waves necessary to switch from CP to EP depends on
630 the details of the initial background stratification and wave characteristics,
631 so more studies are needed to fully understand the switching mechanism.
632 This is left for future work and here we merely illustrated this possibility.

633 The effects of non-linearities or of a background zonal current have been
634 studied numerically and we found they have little impact on our results.
635 However, in nature, non-linear evolution can also involve energy transfer
636 to higher vertical modes (Cravatte et al., 2003), a process that was not
637 evaluated in the present framework with one-layer model. Finally, we have
638 also shown that the anomalies that are created generally remain modest so
639 to obtain strong enough anomalies, there must either be strong retroactive
640 amplification or a succession of waves whose effect accumulates.

641 Our results describe several aspects of the evolution of an equatorial
642 Kelvin wave and of its impact on the upper layer density field. It pro-
643 vides an explanation of the continuity between CP and EP El Niño events.
644 However, this is obviously subject to some caution, as the process oriented
645 configuration is very simple and the model relies on many assumptions: ver-
646 tically homogeneous upper (mixed) layer; reduced gravity; validity of the 1D
647 configuration; constant lower layer density reference; no meridional velocity

648 and no background zonal velocity (for the analytical solutions); existence of
 649 a mean background state (stratification), maintained by mean forcings. We
 650 have also linearized the dynamics for the analytical calculations, and for the
 651 retroactive effect of the wave perturbation which has been parameterized in
 652 the form of Newtonian cooling. The ability to switch from CP to EP types
 653 with multiple waves relies on the choice of the initial perturbation and back-
 654 ground structure, so that we cannot claim this result is general. Finally, let
 655 us again mention that this study focuses on the effect of equatorial Kelvin
 656 waves, once they have been triggered by some unbalancing of the mean state,
 657 for instance by anomalous westerly wind bursts in the western part of the
 658 basin. We have not studied the mechanisms responsible for this triggering,
 659 which is also major ingredient of the ENSO process, as it determines the
 660 shape and strength of the initial Kelvin wave.

661 A number of complementary studies can follow from the present results.
 662 First it should be possible to take into account two tracer equations, one
 663 for salt and one for temperature, and evaluate the effect of salinity on the
 664 previous results. It may also be possible to extend the analytical model to
 665 take into account a mean background zonal velocity. At least, as mentioned
 666 above, a thorough numerical study could be performed to evaluate more
 667 precisely the effect of the background advection. The influence of multiple
 668 waves is also a subject of great interest. Previous studies have shown that
 669 the number of Kelvin waves generated by westerly wind bursts is a key factor
 670 in determining the strength and final structure of the temperature anomaly
 671 (see (Menkes et al., 2014)). Admitting that the initial structure generated
 672 by a primary Kelvin wave is of the CP type, the present model can help
 673 evaluate the number, frequency and strength of individual waves to reach
 674 an EP El Niño, including the combination of upwelling and downwelling

675 Kelvin waves (Su et al., 2018).

676 Another possibility is to test the effect of meridional variations, which
677 could play a significant role in the generation of strong EP events (Chen
678 et al., 2016). It may be difficult to generalize the analytical model to a full
679 2D configuration, but simplified solutions (truncated to the first parabolic
680 cylinder functions, see Thual et al., 2016) may be derived to account for 2D
681 effects. Alternatively, it is possible to develop a 2D version of the reduced
682 gravity numerical model (see Appendix A).

683 A further promising and important study is to compare the present for-
684 malism to realistic fields. This can be easily done for the adiabatic version
685 of the model, but if, as expected, diabatic effects are important, one has to
686 estimate the Newtonian cooling parameters α used in the present theory.
687 Diabatic retroactive effects are associated with ocean/atmosphere coupling
688 or mixing processes which depend on the stratification and velocity of the
689 upper layer of the ocean. The latter are indeed modified during the prop-
690 agation of the equatorial Kelvin wave, which modifies the diabatic fluxes.
691 Simple parameterizations exists (see (Barnier, 1998)) that can be used to
692 evaluate ranges for the variations of the α parameters. Preliminary consid-
693 erations (not shown here) reveal that the value chosen for α_o in this article
694 is of the right order of magnitude. Other processes, not represented in the
695 present simplified model and not associated with ocean/atmosphere coupling
696 or mixing processes, have been shown to play a role in the development of
697 El Niño events. These include for example the transfer of energy to higher
698 vertical modes or vertical advection of temperature/density anomalies into
699 the upper mixed layer (Cravatte et al., 2003; Dewitte et al., 2012, 2013), or
700 other 3D effects which are not properly represented in the present simplified
701 configuration. We think most of the latter processes, can be crudely ap-

proximated by Newtonian cooling terms in our model, but their associated α coefficients may be more difficult to evaluate.

As well as being involved in feedbacks, diabatic processes can also be important independently of the equatorial Kelvin wave perturbations. Stochastic events act as additional forcing terms which do not depend on the perturbation characteristics and have been sometimes identified as determinant for the development of strong EP El Niños (Fedorov et al., 2015). Even if the chosen form in Eq. 17 (a Newtonian damping/amplification) is very specific, in practice any effect having some influence on the physical characteristics of the perturbation can be represented by an appropriate choice of α . For example, a negative α^Θ can account for an additional heating event associated with an external process. Thus, even stochastic events could be fitted to the present framework and it would be possible to evaluate whether they can modify the fate (CP or EP and amplitude) of an El Niño event.

Evaluating the effect of climate change on the ratio between CP and EP types is obviously of great interest. Indeed, several oceanic parameters have been modified in the equatorial Pacific. The mean zonal gradient of SST has increased in the recent decades as a result of the strengthening of the Walker circulation (Sohn et al., 2013; England et al., 2014; Karnauskas et al., 2009). Moreover, while an increased ocean stratification and a flatter thermocline are predicted in GCM global warming scenarios (Timmerman et al., 1999; Yeh et al., 2009), the decades after the 1990s have been associated with a sharper thermocline and an increased La Niña-like background pattern (Xiang et al., 2013). The effect of climate change on El Niño events is still debated (see for instance Giese and Sulagna, 2011), but some observations show that more CP events occurred in recent decades (Yeh et al., 2009; Cai et al., 2014). Several studies have related such an increase of

729 CP events to a change in the mean oceanic structure in the equatorial Pa-
 730 cific. Using GCM experiments, Choi et al. (2011) link the increased CP
 731 occurrence to a stronger zonal gradient of mean surface temperature, while
 732 Dewitte et al. (2012) stress changes in the central Pacific vertical stratifi-
 733 cation. The present study shows that if a stronger mid basin density front
 734 (parameter $\partial_x^2 \rho_o$ in Table 1) favors CP events, other parameters have a non-
 735 trivial influence on the El Niño flavor. For example, an increased global
 736 zonal gradient of density/SST in the equatorial Pacific (parameter $\partial_x \rho_o$ in
 737 Table 1) or a shallower thermocline (parameter \overline{H}_o) favors EP events. Our
 738 numerical results (see section 6) underline that feedback effects or the num-
 739 ber, strength or frequency of Kelvin waves, associated with the westerly
 740 wind bursts are also important (see Table 1). The latter effects are asso-
 741 ciated with ocean/atmosphere interactions, not directly represented in the
 742 analytical model, which can also evolve in a changing climate. To our knowl-
 743 edge, previous studies analyzing the effect of climate change on the observed
 744 evolution of El Niño flavor over recent decades have focused on only a few
 745 parameters. Our results advocate for a study involving the combined effects
 746 of all parameters identified in Table 1.

747 Finally, the present results show that knowledge of the details of the
 748 background stratification and of ocean/atmosphere fluxes are both neces-
 749 sary to be able to understand and predict the fate of an ENSO event. This
 750 advocates for the maintenance of a dedicated in situ observation system for
 751 oceanic and atmospheric measurements, which is currently being discussed
 752 in the framework of the TPOS2020 project (Tropical Pacific Observing Sys-
 753 tem, <http://tpos2020.org/>).

754 *Acknowledgments.* This study has been funded by CNES (french space
755 agency; project TOSCA/OSTST “Alti-ETAO”) and the program ”IDEX at-
756 tractivity chairs” from University of Toulouse (“TEASAO” project). We ac-
757 knowledge discussions with Boris Dewitte, Sophie Cravatte, Frédéric Marin,
758 Alexis Chaigneau and Peter Haynes. Peter Haynes’ visit in Toulouse is
759 funded by the “TEASAO” project.

760 **Appendix A. Derivation of the 1D model**

761 Different models, with increasing complexities, can be used to study
762 ENSO (see Anderson and McCreary, 1985; Benestad, 1997; Neelin et al.,
763 1998; Dijkstra and Burgers, 2002). In this hierarchy, the simplest ocean
764 model is a 1-layer reduced gravity model, whose equations can be written:

$$\begin{aligned}
\partial_t U + U \partial_x U + V \partial_y U - f V &= \frac{1}{\rho_{ref}} \partial_x (g (\rho_s^{tot} - \rho_b) H) + F_x^U, \\
\partial_t V + U \partial_x V + V \partial_y V + f U &= \frac{1}{\rho_{ref}} \partial_y (g (\rho_s^{tot} - \rho_b) H) + F_y^U, \\
\partial_t H + \partial_x (H U) + \partial_y (H V) &= F^H, \\
\partial_t \rho_s + U \partial_x \rho_s + V \partial_y \rho_s &= F^\rho,
\end{aligned} \tag{A.1}$$

765 where $\vec{U} = (U, V)$ is the horizontal velocity field, ρ_{ref} is a constant reference
766 density such that the total density in the mixed layer is $\rho_s^{tot} = \rho_{ref} + \rho_s$.
767 The other terms, \vec{F}^U , F^H and F^ρ , are terms to take into account all effects
768 necessary to explain the evolution of averaged physical quantities in the
769 upper layer using Eq. A.1, in particular it includes all forcing effects (wind
770 stress, vertical mixing, buoyancy/heat flux, effect of instabilities, ...) and
771 parameterizations. If we consider that the lower layer density variation ρ_b
772 is negligible, we can choose $\rho_{ref} = \rho_b$ and Eq. A.1 can be rewritten in the
773 classical form (see for instance Neelin et al., 1998; Dijkstra and Burgers,

774 2002):

$$\begin{aligned}
\partial_t U + U \partial_x U + V \partial_y U - f V &= \partial_x(\Theta) + F_x^U, \\
\partial_t V + U \partial_x V + V \partial_y V + f U &= \partial_y(\Theta) + F_y^U, \\
\partial_t H + \partial_x(H U) + \partial_y(H V) &= F^H, \\
\partial_t \Theta + \partial_x(\Theta U) + \partial_y(\Theta V) &= F^\Theta,
\end{aligned} \tag{A.2}$$

775 where

$$\Theta = g(\rho_s^{tot} - \rho_b) H / \rho_{ref} \simeq g \rho_s H / \rho_{ref} \tag{A.3}$$

776 measures the local buoyancy (\simeq heat) content of the upper layer.

777 In the previous Eq. A.1 or A.2, we hypothesize that -at first order- the
778 upper ocean mixed layer can be represented as a single vertically homoge-
779 neous layer (see Fig. A.15) where physical fields only vary horizontally.

780 Other hypothesis including more complex averaging of the physical fields
781 in the layer are possible, but even though very simplified, the model and
782 Eq. A.2 take into account the continuity equation and the conservation of
783 momentum and buoyancy (or heat). Horizontal advection and the stretching
784 effect associated with the vertical motion of the base of the thermocline
785 ($w(z = -H) = \frac{dH}{dt}$) are taken into account for the evolution of the upper
786 layer thickness and buoyancy content. These are major physical effects for
787 the dynamics of an equatorial Kelvin wave and its impact on the evolution
788 of the density anomaly. Other effects, such as retroactive processes (Ekman
789 feedback or modification of mixing at the base of the thermocline associated
790 with the passage of the wave) are known to be important processes too (Chen
791 et al., 2016). They are associated with the forcing terms F and are not
792 directly represented in the present simplified model but are parameterized
793 as Newtonian cooling terms (see below).

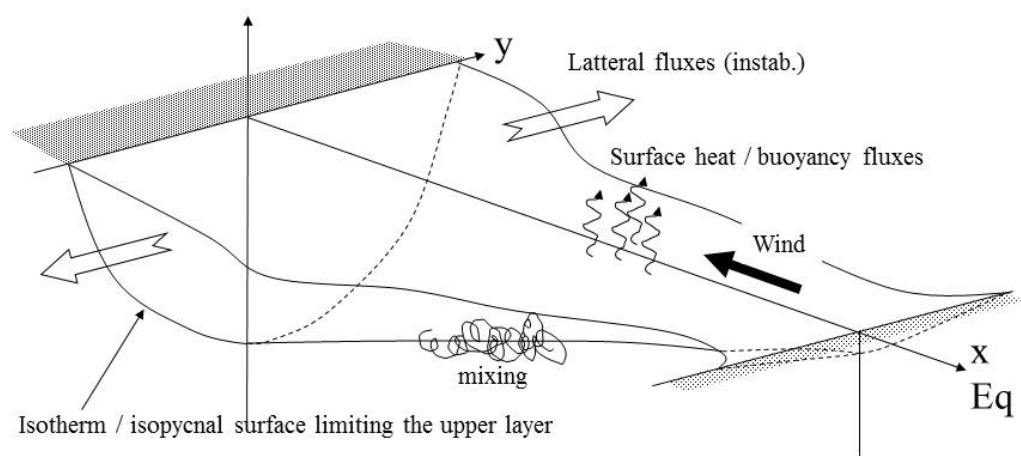


Figure A.15: General view of the mixed layer configuration.

794 To concentrate on equatorial Kelvin wave dynamics in variable environ-
 795 ment along the equator, which is our objective, Eq. A.2 can be further
 796 simplified. Indeed, along the equator, $f = 0$ and the motion is essentially
 797 zonal, so that the meridional component of the velocity can be neglected
 798 ($V \simeq 0$). This is true for equatorial Kelvin waves, and a good approxima-
 799 tion for the mean velocity field. Along the equator we thus get

$$\begin{aligned} \partial_t U + U \partial_x U &= \partial_x \Theta + F^U, \\ \partial_t H + \partial_x (H U) &= F^H, \\ \partial_t (\Theta) + \partial_x (\Theta U) &= F^\Theta, \end{aligned} \tag{A.4}$$

800 which are the final equations we retain for our study.

801 **Appendix B. Equatorial Kelvin Wave solutions for a variable back-** 802 **ground**

803 We have been unable to find exact and general solution for the propaga-
 804 tion of wave in an environment where the equilibrium state varies spatially
 805 and with Newtonian cooling terms. We however propose here an approx-
 806 imate solution which remains quite accurate and allows to estimate the
 807 evolution of the wave amplitude. We linearize Eq. 5 and hypothesize that
 808 $U_o = 0$. The equations simply become:

$$\begin{aligned} \partial_t u &= \partial_x \theta - \alpha^U u, \\ \partial_t \theta &= -\partial_x (\Theta_o u) - \alpha^\Theta \theta. \end{aligned} \tag{B.1}$$

809 We then seek for solutions of the form:

$$\begin{aligned} \theta &= \theta_o e^{-\beta t} e^{i\omega(X(x)-t)}, \\ u &= U(x) \theta. \end{aligned} \tag{B.2}$$

810 Replacing in Eq. B.1 above yields:

$$\begin{aligned} X' &= \frac{i\omega + \beta - \alpha^U}{i\omega} U, \\ \beta + i\omega &= \alpha^\Theta + (\Theta_o U)' + \Theta_o U^2(i\omega + \beta - \alpha^U). \end{aligned} \quad (\text{B.3})$$

811 We then set $Y = \Theta_o U$, $\beta = (\alpha^\Theta + \alpha^U)/2$ and $\gamma = (\alpha^\Theta - \alpha^U)/2$. This yields:

$$Y' + \frac{i\omega + \gamma}{\Theta_o} Y^2 + i\omega - \gamma = 0. \quad (\text{B.4})$$

812 We then hypothesize that $Y = \sqrt{\Theta_o} + \delta Y$ with $\delta Y \ll 1/\sqrt{\Theta_o}$ and that
 813 $\delta Y'$ can be neglected when rederiving the equation for δY . This yields the
 814 approximate solution

$$\delta Y = -\frac{\Theta'_o}{4(i\omega + \gamma)} - \frac{\gamma\sqrt{\Theta_o}}{i\omega + \gamma}, \quad (\text{B.5})$$

815 So that at first order

$$X' \simeq \frac{1}{\sqrt{\Theta_o}} - \frac{\Theta'_o}{4i\omega\Theta_o} \quad (\text{B.6})$$

816 or

$$\begin{aligned} X &\simeq \int \frac{dx}{\sqrt{\Theta_o}} - \frac{1}{i\omega} \text{Log}(\Theta_o^{-1/4}), \\ U &\simeq \frac{1}{\sqrt{\Theta_o}}. \end{aligned} \quad (\text{B.7})$$

817 The approximate solutions for u and θ are then

$$\begin{aligned} \theta &= \theta_o(t=0) e^{-\beta t} \left[\frac{\Theta_o(x=0)}{\Theta_o(x)} \right]^{1/4} \exp[i\omega(x/C - t)], \\ u &= \frac{\theta}{\sqrt{\Theta_o(x)}} = \theta_o(t=0) e^{-\beta t} \frac{\Theta_o(x=0)^{1/4}}{\Theta_o(x)^{3/4}} \exp[i\omega(x/C - t)] \end{aligned} \quad (\text{B.8})$$

where

$$x/C = \int dx / \sqrt{\Theta_o}.$$

818 The solution for the layer depth anomaly h can be derived similarly from
 819 Eq. 5 and B.8, we finally get the following approximate solutions for the
 820 main propagating signal

$$\begin{aligned}\theta &= \theta_o(x/C(x) - t) e^{-(\alpha^\Theta + \alpha^U)t/2} \frac{C_o(x = x_o)^{1/2}}{C_o(x)^{1/2}}, \\ u &= \frac{\theta}{C_o(x)} = \theta_o(x/C(x) - t) e^{-(\alpha^\Theta + \alpha^U)t/2} \frac{C_o(x = x_o)^{1/2}}{C_o(x)^{3/2}}, \\ h &= \frac{\rho_{ref}\theta}{g\rho_o(x)} = \theta_o(x/C(x) - t) e^{-(\alpha^\Theta + \alpha^U)t/2} \frac{\rho_{ref}C_o(x = x_o)^{1/2}}{g\rho_o(x)C_o(x)^{1/2}}\end{aligned}\quad (\text{B.9})$$

821 where θ_o is determined by the -fixed- shape of the initial perturbation, typi-
 822 cally a gaussian function whose maximum θ_o^{max} is given, and x_o is the initial
 823 position of this maximum.

824 The main perturbation propagates at a speed C_o so that at time t the
 825 maximum amplitude is positioned at $\Delta x = C_o t$. The maximum of the main
 826 perturbations as a function of the wave position is thus given by

$$\begin{aligned}\theta &\propto \frac{1}{C_o^{1/2}} e^{-(\alpha^\Theta + \alpha^U)x/2C_o}, \\ u &\propto \frac{1}{C_o^{3/2}} e^{-(\alpha^\Theta + \alpha^U)x/2C_o}, \\ h &\propto \frac{1}{\rho_o C_o^{1/2}} e^{-(\alpha^\Theta + \alpha^U)x/2C_o}.\end{aligned}\quad (\text{B.10})$$

827 Appendix C. Density anomaly evolution

828 The density anomaly is associated with advection and diabatics effects
 829 generated during the passage of the wave. To calculate the density anomaly
 830 ρ associated with a linear wave in a variable environment, we thus have to
 831 use the equation

$$\partial_t \rho = -u \partial_x (\rho + \rho_o) + \frac{\rho_{ref}}{g(h+H_o)^2} [\alpha^H \Theta_o h - \alpha^\Theta H_o \theta + (\alpha^H - \alpha^\Theta) \theta h] \quad (\text{C.1})$$

832 Linearization of the previous equation yields

$$\partial_t \rho = -u \partial_x \rho_o + \frac{\rho_{ref}(\alpha^H - \alpha^\Theta)}{g H_o} \theta. \quad (C.2)$$

833 where θ and $u = \theta/C_o$ are given by Eq. B.9. Thus, starting with a density
834 perturbation which is zero we obtain

$$\partial_t \rho = \left[-\frac{\rho'_o}{C_o^{3/2}} + \frac{\rho_{ref}(\alpha^H - \alpha^\Theta)}{g H_o C_o^{1/2}} \right] e^{-(\alpha^\Theta + \alpha^U)t/2} \theta_o(x/C(x) - t), \quad (C.3)$$

835 which yields using $X = x/C(x) = \int dx/C_o$,

$$\partial_t \rho = A(x) G(X - t) \quad (C.4)$$

836 where

$$\begin{aligned} A(x) &= \left[-\frac{\rho'_o}{C_o^{3/2}} + \frac{\rho_{ref}(\alpha^H - \alpha^\Theta)}{g H_o C_o^{1/2}} \right] e^{-(\alpha^\Theta + \alpha^U)X/2} \\ G(X - t) &= e^{(\alpha^\Theta + \alpha^U)(X-t)/2} \theta_o(x/C(x) - t) \end{aligned} \quad (C.5)$$

837 The solution of Eq. C.4 is

$$\rho(x, t) = A(x) \int_0^t G(X - t') dt'. \quad (C.6)$$

838 or using $T = X - t'$,

$$\rho(x, t) = A(x) \int_{X-t}^X G(T) dT. \quad (C.7)$$

839 Given that the function G is fixed and localized, the integral term is
840 only important to determine the evolution of the density fields in an area
841 where the propagating gravity wave arrives, but once this perturbation has
842 passed, the term remains constant. In the area where the wave has passed,
843 the shape of the density anomaly, which generally also correspond to the
844 maximum anomaly reached during the evolution, is then given by

$$\rho_{max} \propto \left[-\frac{\rho'_o}{C_o^{3/2}} + \frac{\rho_{ref}(\alpha^H - \alpha^\Theta)}{g H_o C_o^{1/2}} \right] e^{-(\alpha^\Theta + \alpha^U)X/2}. \quad (C.8)$$

845 As some forcing fields may only depend on the density anomaly (ρ , and
 846 not on the heat content θ) it is important to generalize Eq. C.2 and add a
 847 Newtonian cooling term depending on the density anomaly alone, to reach:

$$\partial_t \rho = -u \partial_x \rho_o + \frac{\rho_{ref}(\alpha^H - \alpha^\Theta)}{gH_o} \theta + \alpha^\rho \rho. \quad (C.9)$$

848 The right hand side term is the forcing term and is not modified. If
 849 we set $\tilde{\rho} = \rho e^{-\alpha^\rho t}$, $\tilde{\rho}$ verifies Eq. C.2 and we finally get the following
 850 (approximate) solution for ρ

$$\rho_{max} = \left[-\frac{\rho'_o}{C_o^{3/2}} + \frac{\rho_{ref}(\alpha^H - \alpha^\Theta)}{gH_o C_o^{1/2}} \right] e^{-(\alpha^\Theta + \alpha^U)X/2} e^{\alpha^\rho(X-t)} \int_0^t e^{-\alpha^\rho(X-t')} G(X-t') dt' \quad (C.10)$$

851 The same argument as above can be used to state that, since we seek for
 852 the maximum density anomaly reached during the passage of the wave, the
 853 integral term is constant (only depends on the initial shape of the pertur-
 854 bation). To evaluate the influence of the additional $e^{\alpha^\rho(X-t)}$ term, we have
 855 to consider three phases at a fixed location (eulerian view):

- 856 1. as long as the wave does not attain the location, there is no initial
 857 perturbation and the damping term does not act. ρ remains null;
- 858 2. when the wave reaches the location, $t \simeq X$ and the density anomaly
 859 increases because of advection and previous diabatic terms, but the
 860 additional damping term acts during the time of the wave passage
 861 $\Delta t = l_p/C_o$. Thus, in comparison with the case where $\alpha^\rho = 0$, the
 862 maximum density anomaly has to be corrected by a factor $e^{-\alpha^\rho \Delta t} =$
 863 $e^{-\alpha^\rho l_p/C_o}$ so that the maximum density anomaly structure reached just
 864 after the passage of the wave is given by

$$\rho_{max} \propto \left[-\frac{\rho'_o}{C_o^{3/2}} + \frac{\rho_{ref}(\alpha^H - \alpha^\Theta)}{gH_o C_o^{1/2}} \right] e^{-(\alpha^\Theta + \alpha^U)X/2} e^{-\alpha^\rho l_p/C_o}. \quad (C.11)$$

865 3. after the passage of the wave, the forcing term is null and the den-
866 sity anomaly only evolves because of the damping term, so that $\rho =$
867 $\rho_{max}e^{-\alpha\rho(t-t_{max})}$, where $t_{max} \simeq X + l_p/C_o$ is the time at which the
868 wave has left the location.

869 Equation C.11 is the general analytical formula we use for comparison
870 with numerical results.

871 **Appendix D. Model Parameters**

872 Tables for all model parameters.

873 References

- 874 An, S.-I., Jin, F.-F., Aug. 2001. Collective role of thermocline and zonal
875 advective feedbacks in the ENSO mode. *J. Clim.* 14 (16), 3421–3432.
- 876 Anderson, D., McCreary, J., May 1985. Slowly Propagating Disturbances in
877 a Coupled Ocean Atmosphere Model. *J. Atm. Sci.* 42 (6), 615–629.
- 878 Ashok, K., Behera, S. K., Rao, S. A., Weng, H., Yamagata, T., 2007. El
879 nino modoki and its possible teleconnection. *J. Geophys. Res.* 112, 1–27.
- 880 Ashok, K., Yamagata, T., 2009. The el nino with a difference. *Nature* 461,
881 481–484.
- 882 Barnier, B., 1998. Forcing the oceans. Proceeding of the NATO advanced
883 study institute on ocean modelling and parameterization, Kluwer aca-
884 demic publishers, 45–80.
- 885 Bellenger, H., Guilyardi, E., Leloup, J., Lengaigne, M., Vialard, J., 2014.
886 ENSO representation in climate models: from CMIP3 to CMIP5. *Clim.*
887 *Dyn.* 42 (7-8), 1999–2018.
- 888 Benestad, R. E., 1997. Intraseasonal Kelvin Waves in the Tropical Pacific.
889 PhD manuscript, St. Anne’s College, Oxford, United Kingdom, 244 pp.
- 890 Bosc, C., Delcroix, T., 2008. Observed equatorial rossby waves and ENSO-
891 related warm water volume changes in the equatorial pacific ocean.
892 *Journal of Geophysical Research: Oceans* 113 (C6), 1–14.
893 URL <http://onlinelibrary.wiley.com/doi/10.1029/2007JC004613/abstract>
- 894 Busalacchi, A. J., Cane, M. A., 1988. The effect of varying stratification

895 on low-frequency equatorial motions. *Journal of Physical Oceanography*
896 18 (6), 801–812.

897 Cai, W., Borlace, S., Lengaigne, M., van Rensch, P., Collins, M., Vecchi,
898 G., Timmermann, A., Santos, A., McPhaden, M., Wu, L., England, M.,
899 Wang, G., Guilyardi, E., Jin, F.-F., 2014. Increasing frequency of extreme
900 El Nino events due to greenhouse warming. *Nat.Clim.Change* 4, 111–116.

901 Cai, W., Santos, A., Wang, G., Yeh, S.-W., An, S.-I., Cobb, K., Collins,
902 M., Guilyardi, E., Jin, F.-F., Kug, J.-S., Lengaigne, M., McPhaden, M.,
903 Takahashi, K., Timmermann, A., Vecchi, G., Watanabe, M., Wu, L., 2015.
904 Enso and greenhouse warming. *Nat. Clim. Change*, 849–859.

905 Capotondi, A., Wittenberg, A., Newman, M., orenzo, E. D. L., Yu, J.-Y.,
906 Braconnot, P., Cole, J., Dewitte, B., Giese, B., Guilyardi, E., Jin, F.-F.,
907 Karnauskas, K., Kirtman, B., Lee, T., Schneider, N., Xue, Y., Yeh, S.-W.,
908 2015. Understanding ENSO diversity. *Bull. Amer. Meteor. Soc.*, 921–938.

909 Chen, D., Lian, T., Fu, C., Cane, M., Tang, Y., Murtugudde, R., Song, X.,
910 Wu, Q., Zhou, L., May 2015. Strong influence of westerly wind bursts on
911 El Nino diversity. *Nature GeoScience* 8, 339–345.

912 Chen, L., Li, T., Behera, S. K., Doi, T., 2016. Distinctive precursory air–
913 sea signals between regular and super el niños. *Advances in Atmospheric*
914 *Sciences* 33 (8), 996–1004.

915 Chen, L., Li, T., Wang, B., Wang, L., 2017a. Formation Mechanism for
916 2015/16 Super El Niño. *Nature Scientific Reports* 7, 2975.

917 Chen, N., Majda, A., Thual, S., 2017b. Observations and Mechanisms

- 918 of a Simple Stochastic Dynamical Model Capturing El Nino Diversity.
919 J.ClimateAccepted.
- 920 Choi, J., An, S.-I., Kug, J.-S., Yeh, S.-W., 2011. The role of mean state on
921 changes in el niño's flavor. *Climate Dynamics* 37 (5), 1205–1215.
- 922 Clarke, A. J., Jan. 2008. *An Introduction to the Dynamics of El Nino & the*
923 *Southern Oscillation*. Academic Press.
- 924 Clarke, A. J., Van Gorder, S., Colantuono, G., Apr. 2007. Wind stress curl
925 and ENSO Discharge/Recharge in the equatorial pacific. *Journal of Phys-*
926 *ical Oceanography* 37 (4), 1077–1091.
927 URL <http://adsabs.harvard.edu/abs/2007JP0....37.1077C>
- 928 Cravatte, S., Picaut, J., Eldin, G., 2003. Second and first baroclinic kelvin
929 modes in the equatorial pacific at intraseasonal timescales. *Journal of*
930 *Geophysical Research: Oceans* 108 (C8), n/a–n/a, 3266.
931 URL <http://dx.doi.org/10.1029/2002JC001511>
- 932 Dewitte, B., Choi, J., An, S.-I., Thual, S., Jun 2012. Vertical structure
933 variability and equatorial waves during central Pacific and eastern Pacific
934 El Niños in a coupled general circulation mode. *Climate Dynamics* 38 (11),
935 2275–2289.
936 URL <https://doi.org/10.1007/s00382-011-1215-x>
- 937 Dewitte, B., Yeh, S.-W., Thual, S., May 2013. Reinterpreting the thermo-
938 cline feedback in the western-central equatorial Pacific and its relationship
939 with the ENSO modulation. *Clim.Dyn.* 41 (3-4), 819–830.
- 940 Dijkstra, H. A., Burgers, G., 2002. Fluid dynamics of el niño variability.
941 *Annual Review of Fluid Mechanics* 34 (1), 531–558.

942 Dijkstra, H., 2006. The ENSO phenomenon: theory and mechanisms.
943 Adv.Geosciences. 6, 3–15.

944 England, M., McGregor, S., Spence, P., Meehl, G., Timmermann, A., Cai,
945 W., Gupta, A., McPhaden, M., Purich, A., Santoso, A., 2014. Recent
946 intensification of wind-driven circulation in the pacific and the ongoing
947 warming hiatus. Nature Climate Change 4, 222–227.

948 Fedorov, A., Melville, W., 2000. Kelvin Fronts on the Equatorial Thermo-
949 cline. J.Phys.Oceano. 30, 1692–1705.

950 Fedorov, A. V., Hu, S., Lengaigne, M., Guilyardi, E., 2015. The impact
951 of westerly wind bursts and ocean initial state on the development, and
952 diversity of el niño events. Climate Dynamics 44 (5), 1381–1401.

953 Giese, B., Harrison, D., 1990. Aspects of the kelvin wave response to episodic
954 wind forcing. Journal of Geophysical Research 95, 7289–7312.

955 Giese, B. S., Sulagna, R., 2011. El nio variability in simple ocean data
956 assimilation (soda), 18712008. Journal of Geophysical Research: Oceans
957 116 (C2).

958 Gill, A., 1982. Atmosphere-Ocean Dynamics. San-Diego, USA: Academic
959 Press.

960 Guilyardi, E., Wittenberg, A., Fedorov, A., Collins, M., Wang, C., Capotondi, A., van Oldenborgh, G. J., Stockdale, T., 2009. Understanding el
961 nio in ocean atmosphere general circulation models: Progress and chal-
962 lenges. Bull. Amer. Meteor. Soc. 90, 325340.

964 Hirst, A., 1986. Unstable and damped equatorial modes in simple coupled
965 ocean-atmosphere models. J. Atmos. Sci. 43, 606–632.

966 Jin, F.-F., Apr. 1997. An equatorial ocean recharge paradigm for ENSO.
967 part i: Conceptual model. *Journal of the Atmospheric Sciences* 54 (7),
968 811–829.

969 Karnauskas, K. B., Seager, R., Kaplan, A., Kushnir, Y., Cane, M. A., 2009.
970 Observed strengthening of the zonal sea surface temperature gradient
971 across the equatorial pacific ocean. *Journal of Climate* 22 (16), 4316–4321.

972 Kug, J.-S., Choi, J., An, S.-I., Jin, F.-F., Wittenberg, A. T., 2010. Warm
973 Pool and Cold Tongue El Nio Events as Simulated by the GFDL 2.1
974 Coupled GCM. *Journal of Climate* 23 (5), 1226–1239.

975 Kug, J.-S., Jin, F.-F., An, S.-I., 2009. Two types of el nio events: Cold
976 tongue el nio and warm pool el nio. *Journal of Climate* 22 (6), 1499–1515.

977 Liu, Y., Cobb, K., Song, H., Li, Q., Li, C.-Y., Nakatsuka, T., An, Z., Zhou,
978 W., Cai, Q., Li, J., Leavitt, S., Sun, C., Mei, R., Shen, C.-C., Chan, M.-
979 H., Sun, J., Yan, L., Lei, Y., Ma, Y., Li, X., Chen, D., Linderholm, H.,
980 2017. Recent enhancement of central Pacific El Niño variability relative
981 to last eight centuries. *Nature Communications* 8, 15386.

982 Long, B., Chang., P., 1990. Propagation of an Equatorial Kelvin Wave in a
983 Varying Thermocline*. *J.Phys.Oceano.* 20, 1826–1841.

984 Menkes, C. E., Lengaigne, M., Vialard, J., Puy, M., Marchesiello, P., Cra-
985 vatte, S., Cambon, G., 2014. About the role of westerly wind events in
986 the possible development of an el nio in 2014. *Geophys. Res. Let.* 41,
987 6476–6483.

988 Neelin, J. D., Battisti, D. S., Hirst, A. C., Jin, F.-F., Wakata, Y., Yamagata,

989 T., Zebiak, S. E., 1998. ENSO theory. *Journal of Geophysical Research:*
990 *Oceans* 103 (C7), 14261–14290.

991 Paek, H., Yu, J.-Y., Qian, C., 2016. Why were the 2015/2016 and 1997/1998
992 extreme El Ninos different. *Geophys.Res.Lett.* 44, 1848–1856.

993 Picaut, J., Masia, F., du Penhoat, Y., 1997. An advective-reflective concep-
994 tual model for the oscillatory nature of the enso. *Sciences* 277, 663666.

995 Pontaud, M., Thual, O., 1998. Coupled process for equatorial Pacific inter-
996 annual variability. *Q. J. R. Meteorol. Soc.* 124, 527–555.

997 Ren, H.-L., Jin, F.-F., 2013. Recharge oscillator mechanisms in two types of
998 enso. *Journal of Climate* 26 (17), 6506–6523.

999 Sohn, B. J., Yeh, S.-W., Schmetz, J., Song, H.-J., Apr 2013. Observational
1000 evidences of walker circulation change over the last 30 years contrasting
1001 with gcm results. *Climate Dynamics* 40 (7), 1721–1732.

1002 Su, J., Zhang, R., Rong, X., Min, Q., Zhu, C., 2018. Sea surface temperature
1003 in the subtropical pacific boosted the 2015 el niño and hindered the 2016
1004 la niña. *Journal of Climate* 31 (2), 877–893.

1005 Suarez, M. J., Schopf, P. S., 1988. A delayed action oscillator for ENSO.
1006 *Journal of the Atmospheric Sciences* 45 (21), 3283–3287.

1007 Takahashi, K., Montecinos, A., Goubanova, K., Dewitte, B., 2011. Enso
1008 regimes: Reinterpreting the canonical and modoki el nio. *Geophysical*
1009 *Research Letters* 38 (10), n/a–n/a, 110704.
1010 URL <http://dx.doi.org/10.1029/2011GL047364>

1011 Thual, S., Majda, A., Chen, N., Stechmann, S., 2016. A simple stochastic
1012 model for el nino with westerly wind bursts. *Proc. Nat. Acad. Sci. USA*
1013 113, 10245–10250.

1014 Thual, S., Thual, O., Dewitte, B., 2012. Absolute or convective instability
1015 in the equatorial pacific and implications for ENSO. *Quarterly Journal of*
1016 *the Royal Meteorological Society*, n/a–n/a.

1017 Timmerman, A., Oberhuber, J., Bacher, A., Esch, M., Latif, M., Roeckner,
1018 E., 1999. Increased el niño frequency in a climate model forced by future
1019 greenhouse warming. *Nature* 398, 694–696.

1020 Wakata, Y., Sarachik, E., 1991. Unstable Coupled Atmosphere-Ocean Basin
1021 Modes in the Presence of a Spatially Varying Basic State. *J. Atm. Sci.* 48,
1022 2060–2077.

1023 Wang, C., Picaut, J., 2004. Understanding enso physicsa review. *Earths*
1024 *Climate: The Ocean Atmosphere Interaction*, C. Wang, S.-P. Xie, and J.
1025 A. Carton, Eds., Amer. Geophys. Union, 2148.

1026 Wu, D.-H., Anderson, D., 1995. Equatorially trapped basin modes on zonally
1027 varying thermoclines. *Dyn.Atm.Oceans.* 21, 279–294.

1028 Xiang, B., Wang, B., Li, T., 2013. A new paradigm for the predominance of
1029 standing central pacific warming after the late 1990s. *Climate Dynamics*
1030 41 (2), 327–340.

1031 Yang, J., O’Brien, J. J., 1993. A coupled atmosphere-ocean model in the
1032 tropics with different thermocline profiles. *Journal of Climate* 6 (6), 1027–
1033 1040.

- 1034 Yang, J., Yu, L., 1992. Propagation of Equatorially Trapped Waves on a
1035 Sloping Thermocline. *J.Phys.Oceano.* 22, 573–582.
- 1036 Yeh, S.-W., Kug, J.-S., Dewitte, B., Kwon, M.-H., Kirtman, B. P., Jin,
1037 F.-F., 2009. El Nino in a changing climate. *Nature* 461, 511–514.
- 1038 Zebiak, S., Cane, M., May 1987. A Model El Nino-Southern Oscillation.
1039 *Month. Weath. Rev.* 115, 2262–2278.
- 1040 Zheng, Q., Susanto, R., Yan, X.-H., Liu, W., Ho, C.-R., 1998. Observa-
1041 tion of equatorial Kelvin solitary waves in a slowly varying thermocline.
1042 *N.P.Geophys.* 5, 153–165.

Variable	Comments
x : zonal axis	
y : meridional axis	solutions taken at $y = 0$
t : time	
$U = U_o + u$: zonal current	u : anomaly due to the wave
V : meridional current	neglected here
$H = H_o + h$: mixed layer depth	h : anomaly due to the wave
P : pressure	$P \approx g(\rho_b - \rho_s)H$
$\Theta = \Theta_o + \theta$: buoyancy	$\Theta = g(\rho_b - \rho_s)H/\rho_{ref}$, θ : anomaly due to the wave
ρ_s^{tot} : surface density	$\rho_s^{tot} = \rho_{ref} + \rho_s$
$\rho_s = \rho_o + \rho$: surface density variations	ρ is generated by the wave
ρ_b : lower layer density	we choose $\rho_{ref} = \rho_b$
F_x^U : zonal momentum forcing	also noted F^U
F_y^U : meridional momentum forcing	
F^H : mixed layer depth forcing	
F^Θ : buoyancy forcing	
F^ρ : density forcing	
δF : external forcing anomalies	$F^U = F_o^U(x) + \delta F^U(x, t)$, etc

Table D.2: Model variables definitions.

Parameter	Comments
g : gravity	$g = 9.81 \text{ m.s}^{-2}$
f : Coriolis force	$f = 0$ at the equator
U_o : background zonal current	$U_o = 0$ in analytical calculations
L : basin length	$L = 30.000 \text{ km}$
x_o : initial position of wave	
H_o : background depth	$\rho_o = H_{mean} + \Delta H_{max} \frac{x-L/2}{L}$
H_{mean} : mean mixed layer depth	in general $H_{mean} = 120 \text{ m}$
ΔH_{max} : linear depth variation	in general $\Delta H_{max} = 160 \text{ m}$
ρ_{ref} : reference density	1000 kg.m^{-3}
ρ_o : background density	$\rho_o = \rho_{mean} + \Delta \rho_{max}^{lin} \frac{x-L/2}{L} + \Delta \rho_{max}^{th} th((x - x_{th})/L_{th})$
ρ_{mean} : mean mixed layer density	in general $\rho_{mean} = -3 \text{ kg/m}^3$
$\Delta \rho_{max}^{lin}$: linear density variation	$\Delta \rho_{max}^{lin} = 3 \text{ kg/m}^3$ or $= 0.5 \text{ kg/m}^3$
$\Delta \rho_{max}^{th}$: nonlinear density variation	in general $\Delta \rho_{max}^{th} = 0 \text{ kg/m}^3$ or $= 3 \text{ kg/m}^3$
L_{th} : front lengthscale	in general $L_{th} = 5000 \text{ km}$
x_{th} : front position	$x_{th} = L/2$
ρ'_o, ρ''_o : first and second derivatives	$d_x \rho_o, d_x^2 \rho_o$
Θ_o : background buoyancy	$\Theta_o = g \rho_o H_o / \rho_{ref}$
α : Newtonian coolings parameters	$\delta F^U = -\alpha^U u$, etc
C_o : background phase speed	$C_o(x) = \sqrt{-g \rho_o H_o \rho_{ref}}$
C : analytical phase speed	$x/C(x) = \int_{x_o}^x ds/C_o(s)$

Table D.3: Model parameters definitions.